Ionospheric anomalies immediately before M_w 7.0-8.0 earthquakes

Liming He[1,2] & Kosuke Heki[2]

[1]Department of Geodesy and Geomatics, School of Resources and Civil Engineering, Northeastern University, Shenyang, China
[2]Department of Earth and Planetary Sciences, Hokkaido University, Sapporo, Japan

Abstract

Recent observations suggested that ionospheric anomalies appear immediately before large earthquakes with moment magnitudes (M_w) of 8.2 or more. Do similar phenomena precede smaller earthquakes? Here we answer this question by analyzing vertical total electron contents (VTEC) observed near the epicenters before and after 32 earthquakes with M_w7.0-8.0 using data from nearby Global Navigation Satellite System (GNSS) stations. To detect anomalies, we defined the reference curves to fit the observed VTEC, and considered the departure from the curves as anomalies. In estimating the reference curves, we excluded time windows, prescribed for individual earthquakes considering M_w, possibly affected by earthquakes. We validated the method using synthetic VTEC data assuming both pre-, co- and postseismic anomalies. Out of the 32 M_w7.0-8.0 earthquakes, 8 earthquakes showed possible preseismic anomalies starting 10-20 minutes before earthquakes. For earthquakes of this M_w range, we can observe preseismic ionospheric changes probably when the background VTEC is large, say 50 TECU or more.

Key points:

- Ionospheric TEC changes immediately before 8 out of 32 M_w7.0-8.0 earthquakes
- Validation of the reference curve method by numerical tests
- Preseismic ionospheric anomalies emerge when background VTEC is large

1. Introduction: A brief history of the debate

An increasing number of Global Navigation Satellite System (GNSS) receivers continuously operate worldwide near plate boundaries. This makes it possible to observe changes in the ionospheric total electron content (TEC) associated with large earthquakes, and allows us to study coseismic ionospheric disturbances that occur ~10 minutes after earthquakes by acoustic disturbances of the ionosphere [*Calais and Minster*, 1995; *Ducic et al.*, 2003; *Heki and Ping*, 2005; *Astafyeva and Heki*, 2009; *Rolland et al.*, 2013; *Cahyadi and Heki*, 2015]. Such an acoustic disturbance may also cause long-lasting electron depletion above the focal region [*Kakinami et al.*, 2012; *Astafyeva et al.*, 2013; *Shinagawa et al.*, 2013].

Apart from such co- and postseismic ionospheric anomalies, *Heki* [2011] found ionospheric TEC enhancement starting ~40 min before the 2011 M_w9.0 Tohoku-oki earthquake using the Japanese dense GNSS network GEONET (GNSS Earth Observation Network). He also confirmed similar TEC enhancements before the 2004 Sumatra-Andaman (M_w9.2), the 2010

Maule (M_w8.8), and the 1994 Hokkaido-Toho-Oki (M_w8.3) earthquakes, and later the 2007 Bengkulu earthquake (M_w8.5), Southern Sumatra [*Cahyadi and Heki*, 2013]. *Heki and Enomoto* [2015] further added the main shock (M_w8.6) and the largest aftershock (M_w8.2) of the 2012 North Sumatra (Indian Ocean) earthquake, and the 2014 Iquique earthquake (M_w8.2). At this time, the number of earthquakes showing similar precursory ionospheric anomalies became eight, and their M_w ranged from 8.2 to 9.2. They include all the earthquakes with M_w 8.5 or more in this century, with just one exception, the 2005 Nias earthquake (M_w 8.6), where plasma bubble signatures hampered detections of near-field ionospheric disturbances.

Three papers critical to the preseismic ionospheric anomalies have been published [*Kamogawa and Kakinami*, 2013; *Utada and Shimizu*, 2014; *Masci et al.*, 2015]. Their criticisms concentrate on the two points. At first, they consider the preseismic TEC increase an artifact popped up by defining the reference curves using not only the data before earthquakes but also after earthquakes. Secondly, they suspect that the anomalies originate from geomagnetic activities rather than earthquakes.

To rebut the first criticism, *Heki and Enomoto* [2015] proposed a method to confirm statistical significance of the preseismic positive breaks (sudden increases of changing rates) in the vertical TEC (VTEC) trend using the Akaike's Information Criterion (AIC). Recently, *Iwata and Umeno* [2016] proposed a new algorithm to detect preseismic TEC changes by monitoring inter-station correlation of TEC anomalies, which serves as an additional rebuttal to the first criticism. To respond to the second criticism, *Heki and Enomoto* [2015] counted the occurrences of similar changes in VTEC caused by space weather during times of no earthquakes and demonstrated it statistically unrealistic to attribute all the observed VTEC enhancements before large earthquakes to space weather.

Recently, *He and Heki* [2016] analyzed the spatial distribution of preseismic ionospheric anomalies of 3 large earthquakes in Chile, i.e. the 2010 Maule (M_w8.8), the 2014 Iquique (M_w8.2), and the 2015 Illapel (M_w8.3) earthquakes. They found not only positive but also negative anomalies started simultaneously at altitudes of ~200 km and ~400 km, respectively. *Kamogawa and Kakinami* [2013] claim that postseismic electron "decrease" (hole formation) affected the definition of the reference curve and resulted in spurious preseismic "increases". Obviously, the postseismic hole cannot explain simultaneous starts of artificial preseismic anomalies of both polarities. *He and Heki* [2016] also pointed out that the three-dimensional structure of the positive and the negative anomalies along the geomagnetic field is consistent with the ionospheric response to positive electric charges on the ground [*Kuo et al.*, 2014].

M_w dependence of the anomalies would provide another support for the reality of the anomalies as earthquake precursors. We have reported three kinds of such dependence so far. At first, *Heki and Enomoto* [2015] found that the amount of the preseismic VTEC rate changes depend on M_w and background VTEC, i.e. larger precursors occur before larger earthquakes under similar background VTEC. Secondly, *Heki and Enomoto* [2015] found that earthquakes with larger M_w tend to have longer precursor times (i.e. tend to start earlier). Third, *He and Heki* [2016] showed that the anomalies of larger earthquakes have larger spatial dimensions.

Heki and Enomoto [2015] studied earthquakes with $M_w \geq 8.0$ (precursors emerged only before earthquakes with $M_w \geq 8.2$). Past studies all focused on the existence of preseismic anomalies for very large earthquakes, and paid little attention to the "inexistence" of such anomalies for smaller earthquakes. The purpose of the present work is to clarify the lower limit of M_w of earthquakes showing preseismic TEC anomalies. To achieve this goal, we investigate behaviors of VTEC immediately before and after 32 earthquakes worldwide with M_w7.0-8.0 in this century.

2. Data processing

2.1 Extraction of VTEC from GNSS data

In this paper, we use data from Global Positioning System (GPS) satellites. Each GNSS station receives two L-band microwave signals. Due to the dispersive nature of the ionosphere, delays occur between the two carrier waves, and we can convert such delays to numbers of electrons along the line-of-sight (LOS), often called as slant TEC (STEC). We use the unit TECU (TEC Unit), equivalent to 10^{16} electrons/m^2. We derived and removed inter-frequency biases (IFBs) of satellites and stations following *He and Heki* [2016].

Although TEC is an integrated value, we often assume a thin layer at a certain height and calculate the position of the intersection of LOS with this layer, called ionospheric piercing point (IPP). We plot TEC values onto maps using its surface projection, called sub-ionospheric point (SIP). In this paper, we take the height of the layer at the maximum ionization height (~300 km) when we convert STEC to VTEC by multiplying with the cosine of the incident angle of LOS with this thin layer. However, we assume the height at 200 km to draw SIP tracks on the map considering the approximate heights of positive anomalies inferred by *He and Heki* [2016]. We estimate the accuracy of VTEC derived in the present study as ~0.02 TECU [*Coster et al.*, 2013].

2.2 Detection of anomalies

For large earthquake with M_w8.2 or more, *Heki and Enomoto* [2015] showed that detection of positive breaks (sudden increases in rate) using AIC is useful. There we set up a moving time window, spanning 20-40 minutes, and compare AIC between the two cases, (1) fit one line to the whole portion within the window, and (2) split the window into two, and fit two lines with a break at the center. If AIC in (2) is smaller, we consider there was a significant trend change at the center of the window.

It is rather difficult to do this before $M_w \leq 8.0$ earthquakes. In fact, the empirical relationship (Fig.4 of *Heki and Enomoto* [2015]) suggests that the VTEC rate change for $M_w \leq 8$ events are less than 2 TECU/h under moderate background VTEC (e.g. 20 TECU) in mid-latitudes. Then, the short (<20 minutes) precursor times causes a problem, i.e. we need a larger moving time window for a robust detection of small trend changes, (see Fig. 3 of *Heki and Enomoto* [2015]). This becomes difficult for earthquakes with short precursor times.

On the other hand, $M_w \leq 8.0$ earthquakes have a certain benefit that makes it easier to define the reference curves. Their short precursor times and small dimensions of the anomalies make it easier to connect the VTEC curves smoothly before and after the series of pre-, co- (acoustic disturbance), and postseismic (electron depletion) ionospheric disturbances (Figure 1). Here, we model the temporal variations of the VTEC over 2-3 hours periods using polynomials of time (we discuss the selection of the optimum degree in Section 6). We then estimate the reference curves using the VTEC data in this period excluding a certain time window (excluding window), possibly influenced by earthquakes. We then define departures of the observations from the reference curves during the excluding window as the VTEC anomalies.

2.3 Excluding windows

This “reference curve method” is employed in *Heki* [2011], which has been criticized repeatedly by opponents [e.g. *Kamogawa and Kakinami*, 2013]. However, here we adopt two new approaches. At first, we convert STEC to VTEC beforehand, to remove U-shaped apparent changes due to the satellite elevation changes. This makes it easier to see the net increase and decrease intuitively. Secondly, we set up a-priori excluding windows for individual earthquakes. A shorter excluding window would stabilize the estimation of the reference curve. At the same time, the window needs to be long enough to cover the whole sequence of ionospheric disturbances of the studied earthquake.

We set up the start of the excluding window at a certain time between –20 minutes (M_w8.0) and –10 minutes (M_w7.0) relative to earthquakes. *Heki and Enomoto* [2015] showed that onset of the preseismic VTEC anomalies is ~40 minutes before M_w9 class interplate earthquakes, and ~20 minutes before M_w8 class interplate earthquakes. Here we assume that they start ~10 minutes before M_w7 earthquakes. Then we interpolated for the start of the excluding window for earthquakes with M_w between 7.0 and 8.0 (Table S1). Figure 1 shows a conceptual model of typical pre-, co- and postseismic ionospheric anomalies for an earthquake of this M_w range. In Figure 1a, we assume that the preseismic positive anomaly, possibly of electromagnetic origin, starts at $t = -15$ (15 minutes before earthquake). We further assumed that it linearly increases and reaches the maximum at $t = 0$, and decays linearly to zero at $t = 15$.

The end of the excluding window was also set up considering the M_w of the earthquakes. We gave the ending time from +30 minutes (M_w8.0) to +17 minutes (M_w7.0) relative to the earthquake occurrence times. In Figure 1b, acoustic origin coseismic ionospheric disturbances occur at $t = 8$ (8 minutes after earthquakes), as a short positive pulse lasting for 2 minutes, and a postseismic long-duration negative anomaly (hole formation) starts at $t = 10$. Actually, the postseismic ionospheric holes may last for hours for M_w9 earthquakes [*Shinagawa et al.*, 2013]. However, its areal extent would follow the fault size, and would not largely exceed 100/30 km (typical fault sizes of M_w8/7 earthquakes) for M_w8/7 earthquakes. Then, its signature would decay within 20/6 minutes in the observed TEC. This is because LOS takes less than 20/6 minutes to move from the center to the limb of the hole of ~100/30 km diameter made by M_w8/7 earthquakes.

As shown in Figure 1c, the time required for LOS to move out of the hole decreases as the satellite goes farther from the zenith. After all, 30/16 minutes after earthquakes would be late enough to end the excluding window for M_w8/7 earthquakes (Table S1). In the next section, we do simple numerical experiments to confirm the validity of the reference curve method to identify preseismic VTEC anomalies for M_w7-8 earthquakes.

3. Numerical test using synthetic VTEC data

Acoustic waves from epicenters arrive at the F region of the ionosphere in 8-10 minutes, and make coseismic ionospheric disturbances characterized by N-waves. Long-lasting postseismic ionospheric holes often follow these coseismic disturbances [*Kakinami et al.*, 2012; *Shinagawa et al.*, 2013]. Such a postseismic TEC drop could influence the process to derive the reference curve and may give rise to spurious preseismic positive TEC anomalies. To test if this really occurs, we use synthetic VTEC data with and without positive anomalies, and fit reference curves to them.

In this study, we define reference curves derived by polynomial fitting to VTEC excluding the prescribed time window, e.g. from 20 minutes before earthquake ($t = -20$) to 30 minutes after earthquake ($t = +30$) for M_w8.0 earthquakes. Then we define VTEC anomalies as the departures from the reference curves. In order to perform a realistic test, we use the actual VTEC data obtained by observing GPS Satellite 8 at the IGS station AIRA in Kyushu, Japan, 0-2 UT on August 15, 2016, as the platform on which we add artificial anomalies. We utilize a sum of functions representing the pre-, co- and postseismic ionospheric anomalies as illustrated in Figure 1.

We synthesize the observation data for the following two cases, (Case 1) only co- and postseismic acoustic perturbations occur, (Case 2) preseismic TEC anomalies in addition to the co- and postseismic perturbations. In the synthetic data, we assume that the earthquake occurred at 1:00 UT and that the coseismic positive pulse starts 8 minutes after the earthquake and last for 2 minutes. Then the postseismic depletion (hole) appears, and LOS goes out of the hole in 20 minutes (the hole itself remains). We fit the data with the polynomial with degree 3, excluding the time window from –20 minutes to +30 minutes as shown by the gray bar above the time series.

Figure 2a demonstrates that Case 1 does not give rise to spurious preseismic anomalies, i.e. the reference curve overlaps with the data during the preseismic 20 minutes (although we excluded this portion in estimating the reference curve). Figure 2b shows the Case 2, where we assumed all the pre-, co-, and postseismic anomalies. By fitting a reference curve, both positive preseismic and negative postseismic anomalies emerged as departures from the curve. In both cases, we only see anomalies that we assumed, i.e. no artificial anomalies emerge.

Then, in what situation does the spurious preseismic positive anomaly emerge? Figure 2c shows an unrealistic case (Case 3) in which the postseismic hole is so large that the LOS cannot escape from the hole until the end of the time series. This situation makes the VTEC drop continue beyond t =+30, and results in an artificial preseismic enhancement. However, this never really happens for M_w8.0 earthquakes because GPS satellites apparently move in the sky and the horizontal extents of the holes would not largely exceed the size of the ruptured faults, i.e. ~100 km.

4. Earthquakes

Here we explore preseismic VTEC changes for earthquakes with M_w 7.0-8.0. For this purpose, we examine VTEC time series observed at GNSS stations near epicenters immediately before and after earthquakes. Considering the availability of GNSS stations close to epicenters (within ~300 km), we selected 32 M_w7.0-8.0 earthquakes worldwide with focal depths less than 60 km. Figure 3 illustrates locations of these earthquakes, and the inset shows the distribution of their focal depths. Table 1 summarizes detailed information on these earthquakes, where M_w, occurrence time (both in UT and LT), location (geographic longitude and latitude), and depth, are taken from the United States Geological Survey (USGS) catalog. We derived the background VTEC values from the nearby GPS station-satellite pairs shown in the round brackets in italics. We also used those pairs to infer the optimum degrees of polynomials with the L-curve method (Figure S3). We identified possible preseismic ionospheric anomalies in 8 events, marked with circles in the rightmost column of Table 1, out of the 32 earthquakes. In the next chapter, we show the 24 cases without anomalies. After that, we show the 8 cases with possible preseismic anomalies.

Table 1. List of earthquakes studied here.

M_w	Earthquake Region	Date (Y/M/D)	Time (UT)	Time (LT)	GLON (°E)	GLAT (°N)	Depth (km)	Background VTEC (TECU) [c]	Polynomial Degree[d]	Precursor[e]
8.0[a]	Tokachi-oki, Japan	2003/09/25	19:50	04:50	143.9	41.8	27	12 (*0785,04*)	6	x
7.9	Bengkulu, Indonesia[b]	2007/09/12	23:49	06:49	100.8	-2.6	35	7 (*tiku,21*)	5	x
7.9	Denali, Alaska	2002/11/03	22:12	13:12	-147.4	63.5	5	23 (*eil1,29*)	4	x

7.8	Ecuador	2016/04/16	23:58	18:58	-79.9	0.4	21	32 (*riop,30*)	7	O
7.8	Gorkha, Nepal	2015/04/25	06:11	11:56	84.7	28.2	8	63 (*lck4,26*)	7	O
7.8	New Zealand	2009/07/15	09:22	21:22	166.6	-45.8	12	10 (*vgmo,20*)	6	O
7.7	Iquique, Chile[b]	2014/04/03	02:43	23:43	-70.5	-20.6	22	60 (*atic,13*)	4	O
7.7	Antofagasta, Chile	2007/11/14	15:40	12:40	-69.9	-22.2	40	17 (*ctlr,11*)	7	x
7.7	El Salvador	2001/01/13	17:33	11:33	-88.6	13.0	60	53 (*guat,31*)	5	x
7.6	Costa Rica	2012/09/05	14:42	08:42	-85.3	10.1	35	38 (*vera,23*)	4	x
7.6	Colima, Mexico	2003/01/22	02:06	20:06	-104.1	18.8	24	13 (*zihp,23*)	5	x
7.6	Southern Peru[b]	2001/07/07	09:38	04:38	-72.1	-17.5	33	4 (*areq,27*)	6	x
7.5	Papua New Guinea	2015/05/05	01:44	11:44	151.9	-5.5	55	57 (*pngm,15*)	4	O
7.5	Papua New Guinea	2015/03/29	23:48	09:48	152.6	-4.7	41	54 (*pngm,10*)	7	O
7.5	Coastal Alaska	2013/01/05	08:58	23:58	-134.7	55.4	10	7 (*ab48,28*)	6	x
7.4	Oaxaca, Mexico	2012/03/20	18:02	12:02	-98.2	16.5	20	40 (*ineg,21*)	8	O
7.4	Maule, Chile[b]	2010/02/27	08:01	05:01	-75.0	-37.8	35	13 (*conz,13*)	4	x
7.4	Kii Peninsula, Japan	2004/09/05	14:57	23:57	137.1	33.2	10	4 (*0366,20*)	3	x
7.4	Tokachi-oki, Japan[b]	2003/09/25	21:08	06:08	143.6	41.8	33	10 (*0194,27*)	6	x
7.3	Gorkha, Nepal[b]	2015/05/12	07:05	12:50	86.1	27.8	15	80 (*bmcl,19*)	5	O
7.3	El Salvador	2014/10/14	03:51	21:51	-88.1	12.5	40	11 (*ssia,22*)	3	x
7.3	Tohoku-oki, Japan[b]	2011/03/09	02:45	11:45	142.8	38.4	32	23 (*usud,07*)	6	x
7.2	Tajikistan	2015/12/07	07:50	12:50	72.9	38.2	22	13 (*tash,21*)	7	x
7.2	Araucania, Chile	2011/01/02	20:20	17:20	-73.3	-38.4	24	13 (*pecl,09*)	2	x
7.2	Baja Cal., Mexico	2010/04/04	22:40	15:40	-115.3	32.3	10	6 (*p066,32*)	7	x
7.2	Kii Peninsula, Japan[b]	2004/09/05	10:07	19:07	136.6	33.1	14	9 (*0684,15*)	7	x
7.1	Southern Peru	2013/09/25	16:42	11:42	-74.5	-15.8	40	44 (*atic,08*)	8	x
7.1	Central Chile	2012/03/25	22:37	18:37	-72.2	-35.2	41	14 (*cauq,03*)	5	x
7.1	Tohoku, Japan[b]	2011/04/07	14:32	23:32	141.6	38.3	42	12 (*g105,16*)	8	x
7.0	Kumamoto, Japan	2016/04/15	16:25	01:25	130.8	32.8	10	1 (*0087,19*)	2	x
7.0	New Zealand	2010/09/03	16:35	04:35	171.8	-43.5	12	14 (*waim,04*)	7	x
7.0	Haiti	2010/01/12	21:53	16:53	-72.6	18.4	13	17 (*gtk0,29*)	7	x

[a]M_w from *Ozawa et al*. [2004], [b]Aftershocks and foreshocks, [c]Background VTEC value with unit of TECU (*Station name, GPS satellite number*), [d]Degree of polynomials used to define reference curves of VTEC, [e]Existence of preseismic VTEC changes O: VTEC increases are observed. x: No preseismic VTEC anomalies are observed.

5. Earthquakes without preseismic ionospheric VTEC anomalies

He and Heki [2016] showed that the positive electron density anomalies occur around the height of ~200 km at the horizontal location shifted from epicenters toward the equator (those of the 2014 Iquique earthquake, close to the magnetic equator, emerged just above the epicenter). They also showed that the horizontal dimension of the positive anomalies for M_w8.2-8.3 earthquakes do not exceed 500 km. Hence, those for M_w7-8 earthquakes would be smaller. We focus on the identification of the positive anomalies in this study in the expected region using available GNSS data, considering that the negative anomalies are more diverse and lie at higher altitudes [*He and Heki*, 2016].

First, we show VTEC data for the 24 earthquakes marked with symbol "x" in Table 1. For these earthquakes, we did not find significant preseismic ionospheric VTEC changes within expected regions. In Figure 4 (12 earthquakes with larger M_w) and S1 (12 earthquakes with smaller M_w), we present VTEC time series observations near the epicenters of individual earthquakes. The corresponding SIP trajectories (we assumed the thin layer at the height of 200 km) in Figure 5 and S2, respectively.

Figure 4 and S1 shows that the reference curves mostly overlap with the observed VTEC curves over the whole studied periods although we excluded the time windows, e.g. from –20 minutes to +30 minutes relative to the earthquakes for M_w8.0 earthquakes, to derive the reference curves. In this study, we search for the preseismic anomaly as the continuous positive departure of the VTEC from the reference curve, exceeding 0.2 TECU, starting 10-20 minutes before the earthquake, and lasting at least until the earthquake occurred. Hence, we consider there were no significant preseismic TEC anomalies for these 24 earthquakes. This also suggests that we could connect the naturally varying VTEC smoothly with a single polynomial across the time gap of up to 50 minutes.

For many of the 24 earthquakes without preseismic anomalies, we detected coseismic ionospheric disturbances, e.g. the 2003 Tokachi-oki, the 2007 Bengkulu aftershock, and the 2004 Kii Peninsula (both mainshock and foreshock) earthquakes, and they are studied in *Cahyadi and Heki* [2015]. However, we did not find any examples where only postseismic TEC drops are evident. This suggests that the postseismic ionospheric hole has a similar lower limit of M_w and background VTEC to the preseismic anomalies.

In the 24 examples shown in Figures 4-5 and S1-2, insufficient number of GNSS stations may let us fail to capture precursory TEC changes that occurred in regions smaller than expected. Here we highlight the case of the largest earthquake without precursors studied here, i.e. the 25 September 2003 Tokachi-oki earthquake (M_w8.0), Japan, using the data from a dense GNSS array GEONET (GNSS Earth Observation Network). For this earthquake, *Heki and Ping* [2005] and *Rolland et al.* [2011] reported the propagation of coseismic ionospheric disturbances. We selected data with two GPS satellites closest to the local zenith of the studied region. We show the VTEC anomalies at 3 epochs, 20 minutes, 10 minutes, and immediately before earthquakes in Figure 6. We expect that precursory TEC increases may appear to the south of the epicenter. However, we do not recognize significant anomalies there.

6. Earthquakes with preseismic ionospheric VTEC anomalies

Second, we show VTEC data for the eight earthquakes marked with "O" in Table 1. For these earthquakes, we found possible preseismic ionospheric VTEC enhancement (and decrease for one earthquake) in the VTEC observed at nearby GNSS stations. In the following sections, we present VTEC time series for individual earthquakes in a decreasing order of M_w, and the corresponding SIP trajectories drawn assuming the thin layer at the height of 200 km.

In deriving the reference curves, we assume the exclusion windows in the same way as cases without preseismic anomalies. We recognize that there is an arbitrariness in the selection of polynomial degree of the reference curves. In fact, behaviors of the residual within the excluding windows depend on the polynomial degrees. We show two cases in Figure 7, the 2009 New Zealand earthquake (M_w7.8) and the 2015 March Papua New Guinea earthquake (M_w7.5). In the former case, the post-fit residuals show a sudden decrease for degree 4 (Figure 7a inset), and we considered 4 the appropriate degree (in Figure S3, we show the root-mean-squares of the post-fit residuals for all the 32 earthquakes). The background VTEC shows a simple increase (Figure 7a), and the residuals remain consistent for most of the degrees (Figure 7b). The residuals keep positive during the 12-minute period before the earthquake, and we consider that a VTEC anomaly preceded this earthquake.

The VTEC in the latter case, however, shows a strong curvature reflecting the passage of the LOS through the equatorial ionization anomaly (Figure 7c). The shape of the residual during the excluding window depends largely on the polynomial degree (Figure 7d). From the behavior of the residual, we considered 7 the appropriate degree (Figure 7c inset). There the residual during the excluding window exhibit persistent positive values, and we consider that a preseismic VTEC anomaly occurred.

Another arbitrariness may arise from the selection of the total time span (2-3 hours). We find this correlates with the optimal polynomial degree, i.e. a slightly longer window results in a slightly larger polynomial degree. However, the shape of the residual during the excluding window does not depend largely on the total time span.

6.1 The April 16, 2016, Ecuador earthquake (M_w7.8)

The most recent earthquake studied here is the M_w7.8 Pedernales, Ecuador, earthquake, South America, which occurred on 16 April 2016 [*Ye et al.*, 2016]. It ruptured the plate interface where the Nazca Plate subducts beneath the South American Plate. The epicenter is located in northwest Ecuador, at a depth of ~21 km. Three IGS GNSS stations were available in Quito (qui3 and qui4) and Riobamba (riop) of Ecuador (Figure 8b). As seen in Figure 8a, four station-satellite pairs show possible ionospheric VTEC enhancements. The onset time was ~17 minutes before the earthquake. We inferred the VTEC rate change as 1.75 TECU/h by comparing rates during the 10 minutes intervals before and after the break using data from the pair of RIOP and GPS satellite 30. There are postseismic drop (ionospheric hole formation) signatures for all the VTEC curves. However, the LOS would have gone out of the hole before the end of the excluding window (26 minutes after earthquake in this case), and we consider the detected increase real (Case 2 in Figure 2).

6.2 The April 25, 2015, Nepal earthquake (M_w7.8)

The M_w 7.8 Gorkha earthquake occurred on 25 April 2015 in central Nepal, at a depth < 15 km, bringing thousands of casualties in Nepal, India, China, and Bangladesh. This was an interplate earthquake at the diffuse collisional boundary between the Indian and the Eurasian Plates [e.g. *Kobayashi et al.*, 2016]. We downloaded data from 25 GNSS stations near the epicenter from the UNAVCO data center. Figure 9a shows the VTEC curves before and after the earthquake, and those observed at stations in Nepal and northern India using GPS satellites 16 and 26 show clear preseismic enhancements. The focal region is located just beneath the equatorial ionization anomaly (EIA) of the ionosphere, and the earthquake occurred around the local noon. Accordingly, the absolute VTEC was very large and spatially variable in north-south (50-80 TECU). We estimated the VTEC rate change, at ~21 minutes before earthquake, as ~3.1 TECU/h by comparing the rates during the 15 minutes intervals before and after the break using data from the pair of lck4 and GPS satellite 26.

Because the number and distribution of GNSS stations are relatively good for this earthquake, in Figure 9b, we show additional stations farther away from the epicenter which do not show any precursory signals, e.g. smkt and lhaz, in b-1. We can see postseismic TEC drop occurred directly above the fault (e.g. kirt, nast in a-1, and sndl in b-1) while the clearest precursory signals appeared to the west of the fault (e.g. lck4, nagl in a-1).

6.3 The July 15, 2009, New Zealand earthquake (M_w7.8)

A M_w7.8 earthquake struck the west coast of the South Island of New Zealand on July 15, 2009 [*Beavan et al.*, 2010]. It ruptured a transition region from oblique subduction of the Australian Plate beneath the Pacific Plate in the south (the Puysegur Trench) to strike-slip motion further north within the South Island (the Alpine Fault). We used the New Zealand continuous GNSS network, GeoNet, to analyze the VTEC before and after the earthquake.

The background VTEC at the time of the earthquake was only ~10 TECU (Table 1) due to the relatively high magnetic latitude (~50ºS) and nighttime occurrence of the earthquake (21:22 LT). Although *Heki and Enomoto* [2015] suggested it difficult to detect preseismic ionospheric anomalies for a M_w7.8 event under moderate background VTEC, we recognize possible preseismic VTEC enhancements starting ~12 minutes before earthquake with two GPS Satellites 11 and 20 (Figure 10).

6.4 The April 3, 2014, Chile earthquake (M_w7.7, aftershock of the Iquique eq.)

On April 1, 2014, the Iquique earthquake (M_w8.2) ruptured the boundary between the Nazca and the South American Plates around the Peru-Chile border. *He and Heki* [2016] observed significant preseismic ionospheric increases and decreases ~25 minutes before the mainshock. About 27 hours later, the largest aftershock (M_w7.7) occurred ~50 km to the southwest of the mainshock. Here we analyze the VTEC changes before this aftershock using 35 GNSS stations.

We found both preseismic VTEC increase and decrease using GPS Satellites 07, 13, and 23 (Figure 11a), and Satellites 07 and 10 (Figure 11b), respectively, starting at ~14 minutes before earthquake (Figure 11). The spatial distribution of the positive and negative anomalies was similar to the mainshock, i.e. the positive anomaly appeared just above the epicenter, and the negative anomalies emerged both on its north and south sides.

6.5 Two M_w7.5 earthquakes in Papua New Guinea

A pair of M_w7.5 earthquakes occurred beneath the eastern New Britain Island, Papua New Guinea, on 29 March and 5 May, 2015 [*Heidarzadeh et al*., 2015]. This region has a complicated plate tectonic setting, and multiple convergent and divergent boundaries bound numbers of small tectonic blocks lying between the Australian and the Pacific Plates. These two 2015 earthquakes occurred as interplate thrust earthquakes in the New Britain subduction zone.

Although only limited number of GNSS stations were available there, we detected possible preseismic ionospheric enhancements before the first earthquake using GPS Satellite 10 at an IGS site (pngm) in the Manus Island, Papua New Guinea (Figure 12a, also Figure 7b). Similar preseismic ionospheric enhancements occurred before the second earthquake, and was observed using GPS Satellite 15 at the same station (Figure 12b). The onset times for the March and May earthquakes were ~12 minutes and ~14 minutes before earthquakes, respectively.

6.6 The March 20, 2012, Oaxaca earthquake (M_w7.4)

The Oaxaca earthquake of M_w7.4 struck southern Mexico on March 20, 2012 [e.g. *Graham et al.*, 2014]. It was an interplate thrust event at the convergent boundary of the Cocos and the North American Plates. The epicenter is located beneath the state border between Guerrero and Oaxaca at a depth of 20 km. We downloaded data of 18 continuous GNSS stations in Mexico from the UNAVCO data archive to analyze the ionospheric changes before and after this earthquake.

Using the data from GPS satellite 21, we observed weak preseismic VTEC enhancements near the epicenter (Figure 13a). VTEC shows rapid increase during the observation period because the LOS was just entering the EIA. However, the increase is monotonous, and was relatively easy to model. The VTEC residuals show positive anomaly signatures similar to other cases (Figure 13b). The ionospheric VTEC started to increase ~18 min before the earthquake.

6.7 The May 12, 2015, Nepal earthquake (M_w7.3, aftershock of the Gorkha earthquake)

After the M_w7.8 Gorkha, Nepal, earthquake on April 25, 2015, the largest aftershock (M_w7.3) occurred on May 12, 2015. The epicenter of this aftershock, with a depth of ~15 km, was ~140 km away from the mainshock. The background VTEC was very high (~80 TECU). We analyzed the VTEC changes using the GNSS network in Nepal (data available from UNAVCO) and three nearby IGS stations. Possible preseismic VTEC enhancements were observed using two GPS satellites, 19 and 27 (Figure 14). Up to now, this is the earthquake of the smallest M_w with detectable preseismic VTEC anomalies. The onset time was ~14 minute before earthquake.

7. Discussion

7.1 Geomagnetic activities at the times of earthquake occurrences

Heki and Enomoto [2013] showed that the large-scale traveling ionospheric disturbance (LSTID) propagating from auroral ovals often make changes in TEC with similar appearance to preseismic anomalies. Such disturbances occur frequently when geomagnetic activities are high, although *Heki and Enomoto* [2015] demonstrated that they are not frequent enough to account for preseismic TEC enhancements for the earthquakes studied there.

Figure S4 shows the changes of *D*st index before and after the earthquake times for the eight earthquakes with possible preseismic VTEC anomalies. Geomagnetic conditions were quiet for the 2009 New Zealand earthquake (M_w7.8) (Figure S4a), the 2012 Oaxaca earthquake (M_w7.4) (Figure S4b), the 2014 Iquique aftershock (M_w7.7) (Figure S4c), the first 2015 Papua New Guinea earthquake (M_w7.5) (Figure S4d), the 2015 Nepal Gorkha mainshock (M_w7.8), and the second 2015 Papua New Guinea earthquake (M_w7.5) (Figure S4e). On the other hand, when the 2015 Nepal aftershock (M_w7.3) and the 2016 Ecuador earthquake (M_w7.8) occurred, geomagnetic activity was moderately high (*D*st drops were ~29 nT and ~37 nT, respectively) (Figure S4e, f). This activity might be responsible for small-scale undulations in the VTEC time series, but the observations did not deviate seriously from the reference curves within the studied time windows.

In Figure 15, we compare histograms of the *D*st index for all the 32 earthquakes studied here, and for the 8 earthquakes with possible preseismic TEC changes. As a whole, we do not see a significant difference between their distributions, suggesting that there is little correlation between the observed preseismic VTEC anomalies and space weather.

7.2 M_w dependence of preseismic VTEC changes

According to *Heki and Enomoto* [2015], the VTEC rate changes at the onset of the positive preseismic anomalies correlate with two quantities, i.e. earthquake M_w and background VTEC. They proposed an empirical equation based on the data from eight earthquakes with M_w of 8.2 or more. Figure 16 is the leftward-extended version of Figure 4a in *Heki and Enomoto* [2015]. We add the 32 events (8 with precursors and 24 without precursors) studied here. We also add two larger earthquakes, the 2001 June Peru earthquake M_w8.2 (areq and GPS Satellite 30, VTEC rate change is 4.3 TECU/h), and the 2015 September Illapel earthquake M_w8.3 (crzl and GPS Satellite 24, VTEC rate change is 4.0 TECU/h), not included in *Heki and Enomoto* [2015].

We could directly obtain the rate change of VTEC by fitting lines to portions before and after the start of the preseismic increases for the two M_w7.8 earthquakes, the 2015 Nepal and 2016 Ecuador earthquakes. For the other six events with weaker preseismic signals, we did not calculate the rate changes in this way. So we show them using triangles with a uniform size in Figure 16a, and do not include them in Figure 16b,c.

It seems that even for the earthquakes with M_w7.0-8.0, preseismic TEC anomalies may become large enough to be detected if the background VTEC is sufficiently high, say >50 TECU. One may suspect that this simply reflects larger random fluctuations during periods of high background VTEC. In Figure S5, we show this is not the case by comparing VTEC time series over 7 consecutive days including the 2015 Gorkha, Nepal, earthquakes (mainshock in April and the largest aftershock in May). Background VTEC shows persistently large values for all these days (~60 TECU for the mainshock, and ~80 TECU for the largest aftershock). Nevertheless, preseismic anomalies, here defined as persistent departure from the reference curve starting 10-20 minute before earthquakes, only occur on earthquake days.

The two earthquakes, i.e. the 2001 El Salvador earthquake (M_w7.7) and the 2012 Costa Rica earthquake (M_w7.6), showed no significant preseismic ionospheric anomalies although the background VTEC were relatively large (53 and 38 TECU, respectively). For the 2001 earthquake, small numbers of nearby GNSS stations might have simply failed to capture preseismic signals (i.e. no LOS passed through the anomaly). For the 2012 Costa Rica earthquake, VTEC curves seem to show small positive deviations, slightly less than 1 TECU, from -15 to +15 minutes relative to the earthquake (6th panel of Figure 4). They are, however, not so clear as the 8 earthquakes marked with "O" in Table 1.

On the other hand, the 2009 New Zealand earthquake (M_w7.8) showed preseismic VTEC increases although the background VTEC is only ~10 TECU. There may be unknown factors, in addition to M_w and background VTEC, governing the emergence of precursors, e.g. geomagnetic inclinations, land/sea distributions above the focal regions. Our study confirmed that the large background VTEC plays the key role to make ionospheric anomalies immediately before $M_w \leq 8$ earthquakes detectable. After all, the ratio of the occurrence of preseismic TEC anomalies show monotonous decrease for smaller earthquakes (Figure 16a), i.e. the ratio is 100 % for earthquakes with $M_w \geq 8.5$, ~70 % for those with $8.0 \leq M_w < 8.5$, ~40 % for those with $7.5 \leq M_w < 8.0$, and 10 % for $7.0 \leq M_w < 7.5$.

In Figure 17, we compare signatures of preseismic positive VTEC anomalies detected for 8 earthquakes with M_w7.3-7.8 here. They have common features that the anomaly starts 10-20 minutes before earthquakes and terminates by 20-30 minutes after earthquakes. Subtle differences of the signatures come from several factors concerning co- and postseismic ionospheric disturbances. For example, clear coseismic positive pulses appear only in the 2015 March Papua New Guinea case. This is due to the interaction with geomagnetic fields, i.e. clear pulses appear only when the receivers and SIP satisfy a certain geometric condition [see e.g. *Cahyadi and Heki*, 2015]. Because the regions of the preseismic increase and postseismic depletion are different [see e.g. Fig.8 of *Heki and Enomoto*, 2015], some examples show clear postseismic depletion signatures (e.g. 2016 Ecuador) while other examples do not (e.g. 2015 Nepal, mainshock).

Because of the smaller dimensions of preseismic anomalies, the starts of the positive anomalies for M_w7-8 earthquakes may not represent the onsets of preseismic ionospheric changes (i.e. they may rather indicate the entry of LOS into the region of positive anomaly). Nevertheless, we could see that they start between –20 minutes and –10 minutes relative to the earthquakes, and such start times are mostly consistent with the prescribed starts of the exclusion windows (red lines in Figure 17). Figure 17 also suggests a weak correlation between the precursor times and M_w, i.e. the anomalies start earlier for larger earthquakes.

7.3 Physical mechanism of preseismic TEC anomalies

Although we have clear physical interpretations for the coseismic and postseismic ionospheric disturbances [e.g. *Rolland et al.*, 2013; *Shinagawa et al.*, 2013], those for ionospheric anomalies immediately before large earthquakes have not been established. The focus of the present study is the investigation of preseismic TEC anomalies before earthquakes with smaller M_w (7.0-8.0). Nevertheless, it would be meaningful to briefly review recent studies on physical processes responsible for TEC changes immediately before large earthquakes. We consider the anomalies to originate possibly from positive electric charges from stressed rocks, as demonstrated by laboratory experiments [e.g. *Freund*, 2013], and subsequent redistribution of ionospheric electrons [*Kuo et al.*, 2014; *Kelley et al.*, 2017].

Kuo et al. [2014] conducted numerical simulations and demonstrated that the upward electric current into ionosphere could make westward electric field within ionosphere. This causes downward $\boldsymbol{E}\times\boldsymbol{B}$ drift of ionospheric electrons, and redistribution of ionospheric electrons. *He and Heki* [2016] reported that the three-dimensional structure of positive and negative electron density anomalies before the 2015 Illapel earthquake is consistent with *Kuo et al.* [2014]. Recently, *Prokhorov and Zolotov* [2017] pointed out a problem in their numerical treatments of the atmospheric electric currents, and *Kuo and Lee* [2017], in their reply, showed that the problem does not emerge.

In a recent paper, *Kelley et al.* [2017] also hypothesized that electric fields within ionosphere have redistributed electrons by the $\boldsymbol{E}\times\boldsymbol{B}$ drift. They suggested that surface positive charges directly caused electric fields within ionosphere while *Kuo et al.* [2014] considered that upward electric currents need to flow in the atmosphere to make such electric fields. Considering that the ionospheric electric fields need to be ~1 mV/m to explain the observed TEC anomalies, they inferred the electric fields near/on the ground to be ~200 mV/m. This is only ~1/500 of the fair weather electric field.

In either *Kuo et al.* [2014] or *Kelley et al.* [2017], the ionospheric anomalies are driven by positive electric charges from stressed rocks. Hence, the M_w dependence of preseismic TEC anomalies would reflect the M_w dependence (fault size dependence) of the amount and spatial extent of such electric charges, and the occurrence of VTEC rate change would correspond to the onset of the $\boldsymbol{E}\times\boldsymbol{B}$ drift of the electrons. There are certain deviations between real M_w and those calculated from the observed TEC changes and absolute VTEC. For example, the precursor of the 2011 Tohoku-oki earthquake corresponded to M_w8.5 but the real M_w was 9.0. Nevertheless, our studies suggest that final earthquake sizes are, to a large extent, determined before the fast fault ruptures of the main shocks initiate, in opposition to the concept widely accepted by seismologists that earthquakes do not know their final sizes at their starts [e.g. *Ide and Aochi*, 2005].

7.4 Concluding remarks

In this paper, we answered a question if smaller (M_w7.0-8.0) earthquakes also show preseismic changes in ionospheric TEC. We sought the signals in TEC time series before and after 32 recent earthquakes for which nearby GNSS stations recorded TEC in the expected regions for such anomalies (i.e. south/north of the epicenter for northern/southern hemisphere, and just above them for earthquakes close to the magnetic equator).

We find the reference curve method useful for such earthquakes because their precursor times are relatively short (<20 minutes) and the LOS soon go out of the postseismic ionospheric holes. For 24 earthquakes, preseismic VTEC time series smoothly connected to those after earthquakes without significant departures before and after earthquakes although we excluded intervals of prescribed lengths (e.g. from 20 minutes before earthquakes to 30 minutes after earthquakes for M_w8.0 earthquakes) in estimating the reference curves. However, 8 earthquakes showed possible preseismic changes starting 20-10 minutes before earthquakes.

The results suggest the answer is positive, i.e. we can observe them before M_w7.0-8.0 earthquakes. At the same time, we found that they emerge probably when background VTEC are large, say over 50 TECU. Precursor times for these 8 earthquakes are all shorter than 20 minutes. Because these preseismic signals are faint, we would not notice them before earthquakes. Therefore, we do not think this phenomenon useful for practical short-term predictions of M_w7.0-8.0 earthquakes. Nevertheless, this study would provide meaningful information to clarify physical mechanisms underlying electromagnetic phenomena preceding large earthquakes and to pave the way for future short-term prediction of M_w>8.5 earthquakes.

Acknowledgements

We thank constructive comments from the two reviewers. Liming He was supported by the China Scholarship Council (CSC) and by the National Natural Science Foundation of China (Grant no. 41104104). We downloaded the GNSS data mainly from UNAVCO (www.unavco.org), and IGS (garner.ucsd.edu), and partly from other sources including GEONET (www.terras.gsi.go.jp) in Japan, GeoNET (ftp.geonet.org.nz) in New Zealand, RAMSAC (www.ign.gob.ar) in Argentine.

References

Astafyeva, E., and K. Heki (2009), Dependence of waveform of near-field coseismic ionospheric disturbances on focal mechanisms, *Earth Planets Space, 61(7)*, 939-943.

Astavyeva, E., S. Shalimov, E. Olshanskaya, and P. Lognonné (2013), Ionospheric response to earthquakes of different magnitudes: Larger quakes perturb the ionosphere stronger and longer, *Geophys. Res. Lett.*, *40*, 1675-1681, doi:10.1002/grl.50398.

Beavan, J., S. Samsonov, P. Denys, R. Sutherland, N. Palmer, and M. Denham (2010), Oblique slip on the Puysegur subduction interface in the 2009 July Mw7.8 Dusky Sound earthquake from GPS and InSAR observations: implications for the tectonics of wouthwestern New Zealand, *Geophys. J. Int., 183*, 1265-1286, doi:10.1111/j.1365-246X.2010.04798.x.

Cahyadi, M. N., and K. Heki (2013), Ionospheric disturbances of the 2007 Bengkulu and the 2005 Nias earthquakes, Sumatra, observed with a regional GPS network, *J. Geophys. Res. Space Phys.*, *118(4)*, 1777-1787.

Cahyadi, M. N., and K. Heki (2015), Coseismic ionospheric disturbance of the large strike-slip earthquakes in North Sumatra in 2012: M_w dependence of the disturbance amplitudes, *Geophys. J. Int.*, *200(1)*, 116-129.

Calais, E., and J. B. Minster (1995), GPS detection of ionospheric perturbations following the January 17, 1994, Northridge earthquake, *Geophys. Res. Lett.*, *22(9)*, 1045-1048.

Coster, A., J. Williams, A. Weatherwax, W. Rideout, and D. Herne (2013), Accuracy of GPS total electron content: GPS receiver bias temperature dependence, *Radio Sci.*, *48(2)*, 190-196.

Ducic, V., J. Artru, and P. Lognonné (2003), Ionospheric remote sensing of the Denali Earthquake Rayleigh surface waves, *Geophys. Res. Lett., 30(18)*. 1951, doi:10.1029/2003GL017812.

Freund, F. (2013), Earthquake forewarning - A multidisciplinary challenge from the ground up to space, *Acta Geophys., 6(14)*, 775-807, doi:10.2478/s11600-013-0130-4.

Graham, S. E., C. DeMets, E. Cabral-Cano, V. Kostoglodov, A. Walpersdorf, N. Cotte, M. Brudzinski, R. McCaffrey, and L. Salazar-Tlaczani (2014), GPS constraints on the 2011-2012 Oaxaca slow slip event that preceded the 2012 March 20 Ometepec earthquake, southern Mexico, *Geophys. J. Int., 197*, 1593-1607, doi:10.1093/gji/ggu019.

He, L., and K. Heki (2016), Three-dimensional distribution of ionospheric anomalies prior to three large earthquakes in Chile, *Geophys. Res. Lett., 43(14)*, 7287-7293, doi:10.1002/2016GL069863..

Heidarzadeh, M., A. R. Gusman, T. Harada, and K. Satake (2015), *Geophys. Res. Lett., 42*, 5958-5965, doi:10.1002/2015GL064770.

Heki, K. (2011), Ionospheric electron enhancement preceding the 2011 Tohoku-Oki earthquake, *Geophys. Res. Lett., 38*(17), L17312, doi:10.1029/2011GL047908..

Heki, K., and J. Ping (2005), Directivity and apparent velocity of the coseismic ionospheric disturbances observed with a dense GPS array, *Earth Planet. Sci. Lett., 236(3)*, 845-855.

Heki, K., and Y. Enomoto (2013), Preseismic ionospheric electron enhancements revisited, *J. Geophys. Res. Space Phys., 118(10)*, 6618-6626, doi:10.1002/jgra.50578.

Heki, K. and Y. Enomoto (2014), Reply to comment by K. Heki and Y. Enomoto on “Preseismic ionospheric electron enhancements revisited”, *J. Geophys. Res. Space Phys., 119*(7), 6016-6018, doi:10.1002/2014JA020223.

Heki, K., and Y. Enomoto (2015), Mw dependence of the preseismic ionospheric electron enhancements, *J. Geophys. Res. Space Phys., 120*, 7006-7020, doi:10.1002/2015JA021353.

Ide, S. and H. Aochi (2005), Earthquakes as multiscale dynamic ruptures with heterogeneous fracture surface energy, *J. Geophys. Res. Solid Earth, 110*, B11303, doi:10.1029/2004JB003591.

Iwata, T. and K. Umeno (2016), Correlation Analysis for Preseismic Total Electron Content Anomalies around the 2011 Tohoku-Oki Earthquake, *J. Geophys. Res. Space Phys., 121*, 8969-8984, doi:10.1002/2016JA023036

Kakinami, Y., M. Kamogawa, Y. Tanioka, S. Watanabe, A. R. Gusman, J.-Y. Liu, Y. Watanabe, and T. Mogi (2012), Tsunamigenic ionospheric hole, *Geophys. Res. Lett. 39*, L00G27, doi:10.1029/2011GL050159.

Kamogawa, M., and Y. Kakinami (2013), Is an ionospheric electron enhancement preceding the 2011 Tohoku - Oki earthquake a precursor?, *J. Geophys. Res. Space Phys., 118*(4), 1751-1754, doi:10.1002/jgra.50118.

Kelley, M. C., W. E. Swartz, and K. Heki (2017), Apparent ionospheric total electron content variations prior to major earthquakes due to electric fields created by tectonic stresses, *J. Geophys. Res. Space Phys., 122*, doi:10.1002/2016JA023601.

Kobayashi, H., K. Koketsu, H. Miyake, N. Takai, M. Shigefuji, M. Bhattara, and S. N. Sapkota (2016), Joint inversion of telesesimic, geodetic, and near-field waveform datasets for rupture process of the 2015 Gorkha, Nepal, earthquake, *Earth Planets Space, 68*, doi:10.1186/s40623-016-0441-1.

Kuo, C. L., L. C. Lee, and J. D. Huba (2014), An improved coupling model for the lithosphere-atmosphere-ionosphere system, *J. Geophys. Res. Space Phys.*, *119*, 3189-3205, doi:10.1002/2013JA019392.

Kuo, C. L. and L. C. Lee (2017), Reply to comments by B. E. Prokhorov and O. V. Zolotov on "An improved coupling model for the lithosphere-atmosphere-ionospherie system", *J. Geophys. Res. Space Phys.*, *122*, 4869-4874, doi:10.1002/2016/JA023579.

Masci, F., J. Thomas, F. Villani, J. Secan, and N. Rivera (2015), On the onset of ionospheric precursors 40 min before strong earthquakes, *J. Geophys. Res. Space Phys.*, *120*(2), 1383-1393, doi:10.1002/2014JA020822.

Ozawa, S., M. Kaidzu, M. Murakami, T. Imakiire, and Y. Hatanaka (2004), Coseismic and postseismic crustal deformation after the M_w8 Tokachi-oki earthquake in Japan, *Earth, Planets Space*, *56*(7), 675-680.

Prokhorov, B. E., and O. V. Zolotov (2017), Comment on "An improved coupling model for the lithosphere-atmosphere-ionosphere system" by Kuo et al. [2014], *J. Geophys. Res. Space Physics*, *122*, 4865-4868, doi:10.1002/2016JA023441.

Rolland, L. M., P. Lognonné, and H. Munekane (2011), Detection and modelling of Rayleigh wave induced patterns in the ionosphere, *J. Geophys. Res. Space Phys.*, *116*, A05320, doi:10.1029/2010JA016060.

Rolland, L. M., M. Vergnolle, J. M. Nocquet, A. Sladen, J. X. Dessa, F. Tavakoli, H. R. Nankali, and F. Cappa (2013), Discriminating the tectonic and non-tectonic contributions in the ionospheric signature of the 2011, Mw7. 1, dip-slip Van earthquake, Eastern Turkey, *Geophys. Res. Lett.*, *40(11)*, 2518-2522, doi:10.1002/grl.50544.

Shinagawa, H., T. Tsugawa, M. Matsumura, T. Iyemori, A. Saito, T. Maruyama, H. Jin, M. Nishioka, and Y. Otsuka (2013), Two-dimensional simulation of ionospheric variations in the vicinity of the epicenter of the Tohoku-Oki earthquake on 11 March 2011, *Geophys. Res. Lett.*, *40*, 5009-5013, doi:10.1002/2013GL057627.

Utada, H., and H. Shimizu (2014), Comment on "Preseismic ionospheric electron enhancements revisited" by K. Heki and Y. Enomoto, *J. Geophys. Res. Space Phys.*, *119(7)*, 6011-6015, doi:10.1002/2014JA020044.

Ye, L., H. Kanamori, J.-P. Avouac, L. Li, K.F. Cheung, and T. Lay (2016), The 16 April 2016, M_w7.8 (M_s7.5) Ecuador earthquake: A quasi-repeat of the 1942 M_s7.5 earthquake and partial re-rupture of the 1906 M_s8.6 Colombia-Ecuador earthquake, *Earth Planet. Sci. Lett.*, *454*, 248-258, doi:10.1016/j.epsl.2016.09.006.

Figures:

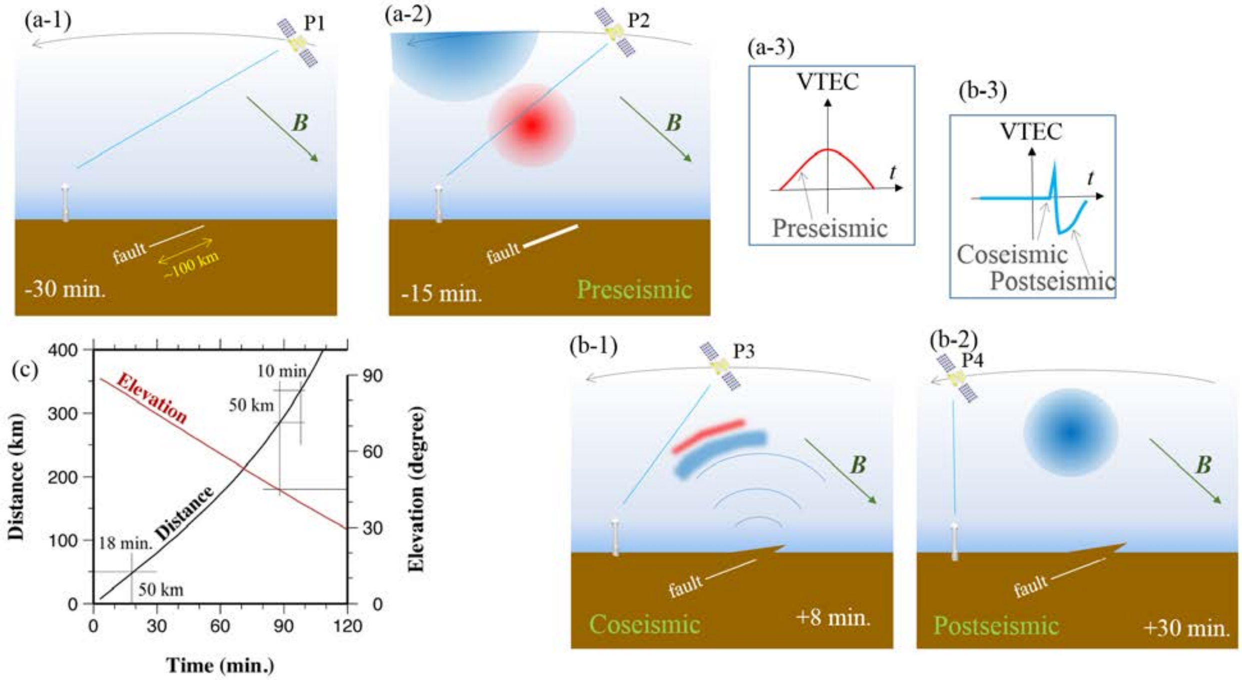

Figure 1. Conceptual sketch of pre-, co-, and postseismic ionospheric anomalies and how they emerge in GNSS-TEC records as the satellite moves from P1 to P4. Ionospheric anomalies that may appear immediately before (a-2) and after (b-1,2) large earthquakes. We assume that preseismic anomalies appear as a pair of compact positive (red) and diverse negative (blue) anomalies, at lower and higher parts of the ionosphere, respectively, along the geomagnetic field ***B***. Here we assume that they start at 15 minutes before an earthquake (t = –15), grow until the earthquake occurs, and decay in 15 minutes after the earthquake (a-1, 2). For a GNSS satellite moving in the sky from P2 to P3 and passing the zenith at the time of earthquakes, such anomalies would make VTEC signatures as shown in (a-3). Eight minutes after the earthquake, the acoustic disturbance arrives at the F region of the ionosphere (b-1), and makes a long-lasting hole (b-2). This series of mechanical disturbances, which we call as coseismic and postseismic anomalies, respectively, will make signatures in VTEC like in (b-3). The earthquake occurrence time is the intersection of X axis (t) and Y axis (VTEC) in (a-3) and (b-3). We further assume that the dimension of the postseismic negative anomaly (blue in b-2) is similar to the fault size, say <100 km for M_w<8 earthquakes. In (c), we show time-distance diagram of IPP at the F region for a GNSS satellite passing the zenith at t = 0. It takes 10-20 minutes for LOS to go from the center to the limb of the hole.

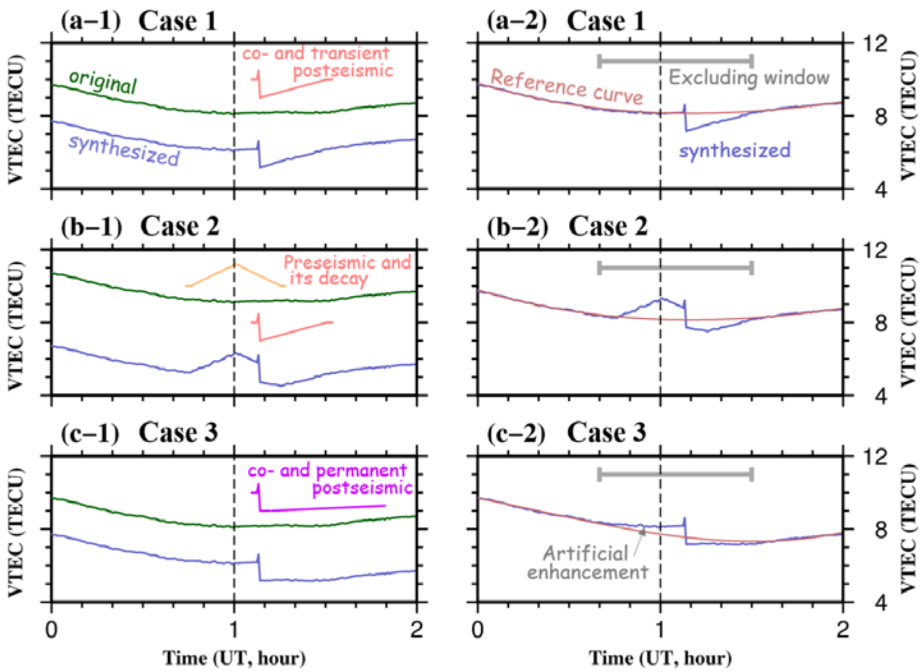

Figure 2. Numerical tests of reference curve fitting for the synthetic VTEC data. The green and blue curves indicate the original VTEC changes and those with additional anomalies related to an earthquake at UT 1:00. For additional anomalies, we consider three cases, (a) Case 1: only co- (acoustic pulse) and postseismic (hole) anomalies, (b) Case 2: preseismic increase in addition to co- and postseismic anomalies, and (c) Case 3: same as (a) but the postseismic hole is large enough to confine LOS within the hole for 1 hour. Red curves in the right panels show the reference curves estimated to fit the VTEC using cubic polynomials of time for the part outside the excluding window shown as gray bars (from –20 minutes to +30 minutes).

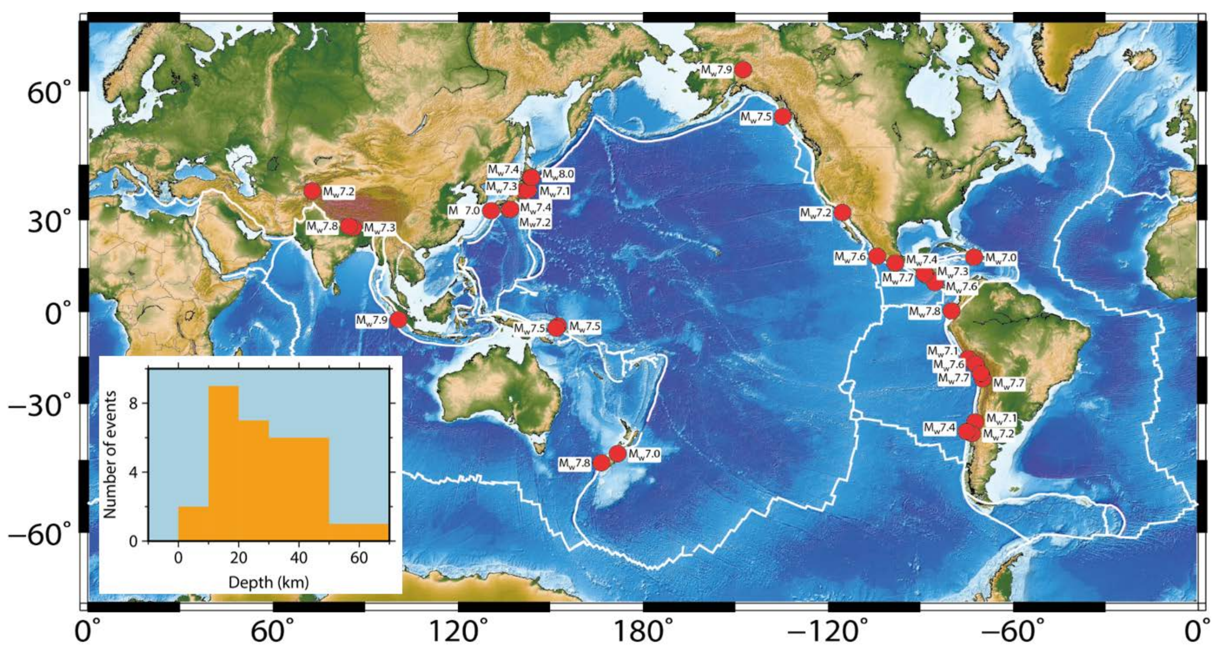

Figure 3. A map showing epicenters of the 32 M_w7.0-8.0 earthquakes studied here (red circles). The inset shows the distribution of the focal depths for all the events.

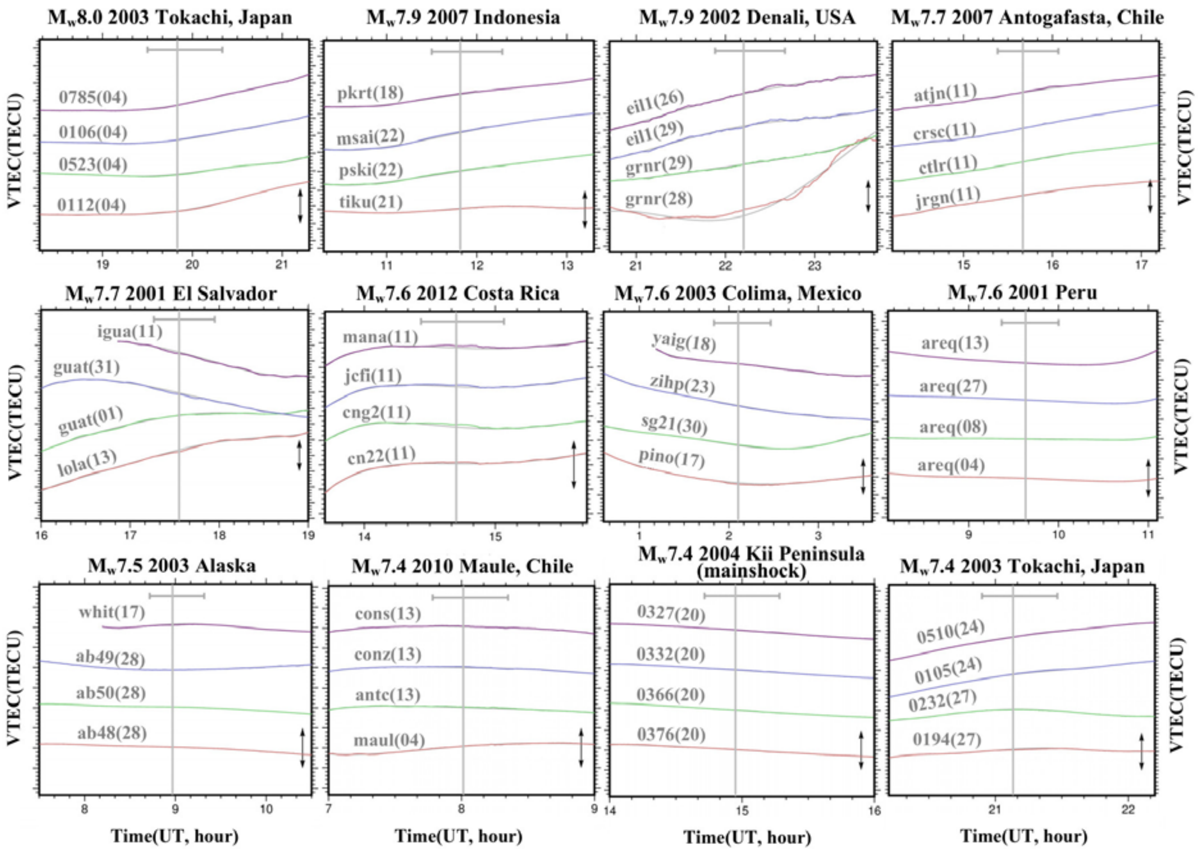

Figure 4. Changes of VTEC over 2-3 hours period obtained from four station-satellite pairs near the epicenter, for 12 of the 24 earthquakes without preseismic anomalies (marked with symbol "x" in Table 1). We show the rest of the earthquakes in Figure S1. The gray horizontal bars represent the excluded time period in defining the reference curves. The gray vertical lines represent the earthquake times. The vertical arrows represent 10 TECU. We list the degree of polynomials used for the reference curves in Table 1.

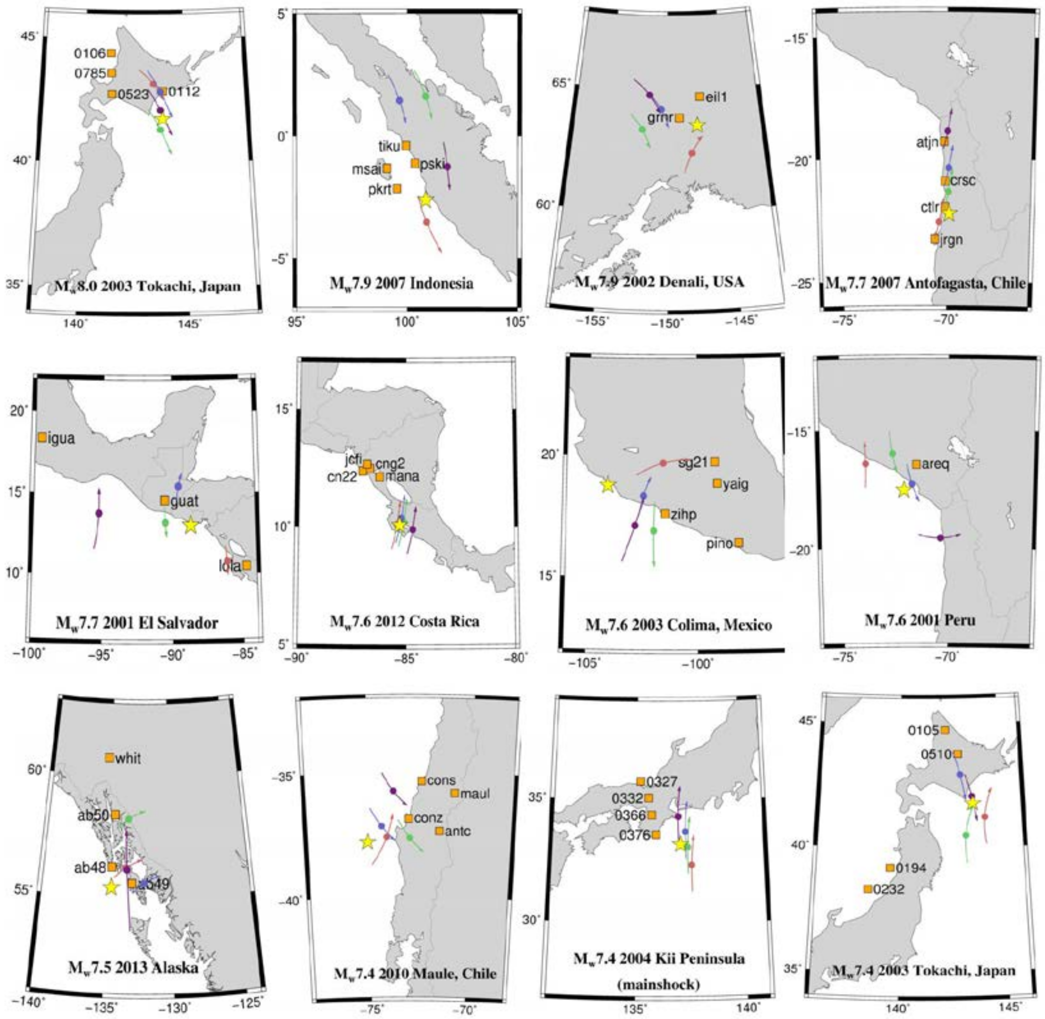

Figure 5. Maps showing the SIP trajectories (the colors correspond to those in Figure 4) calculated assuming the ionospheric height of 200 km for 12 of the 24 earthquakes without precursory TEC changes (marked with symbol ”x” in Table 1). We give similar figures for the rest of the earthquakes in Figure S2. The orange squares show the locations of GNSS stations. The circles on the SIP trajectories show the SIP at the earthquake time. The yellow stars show the epicenters.

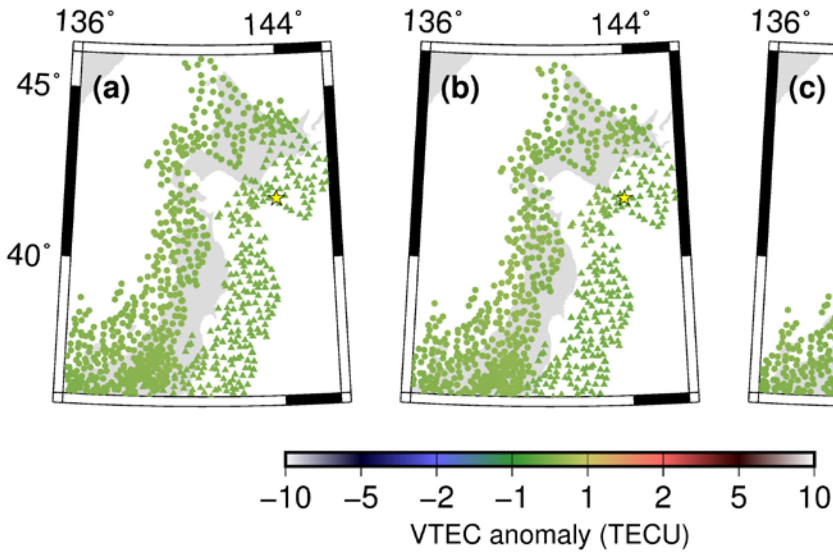

Figure 6. VTEC anomalies at 20 minutes (a), 10 minutes (b) and immediately (c) before the 25 September 2003 M_w8.0 Tokachi-oki earthquake drawn using GPS Satellites 4 (triangle) and 24 (circle). We calculated the SIP positions assuming 200 km as the ionospheric height. The yellow star represents the epicenter. We do not see significant anomalies at any epochs.

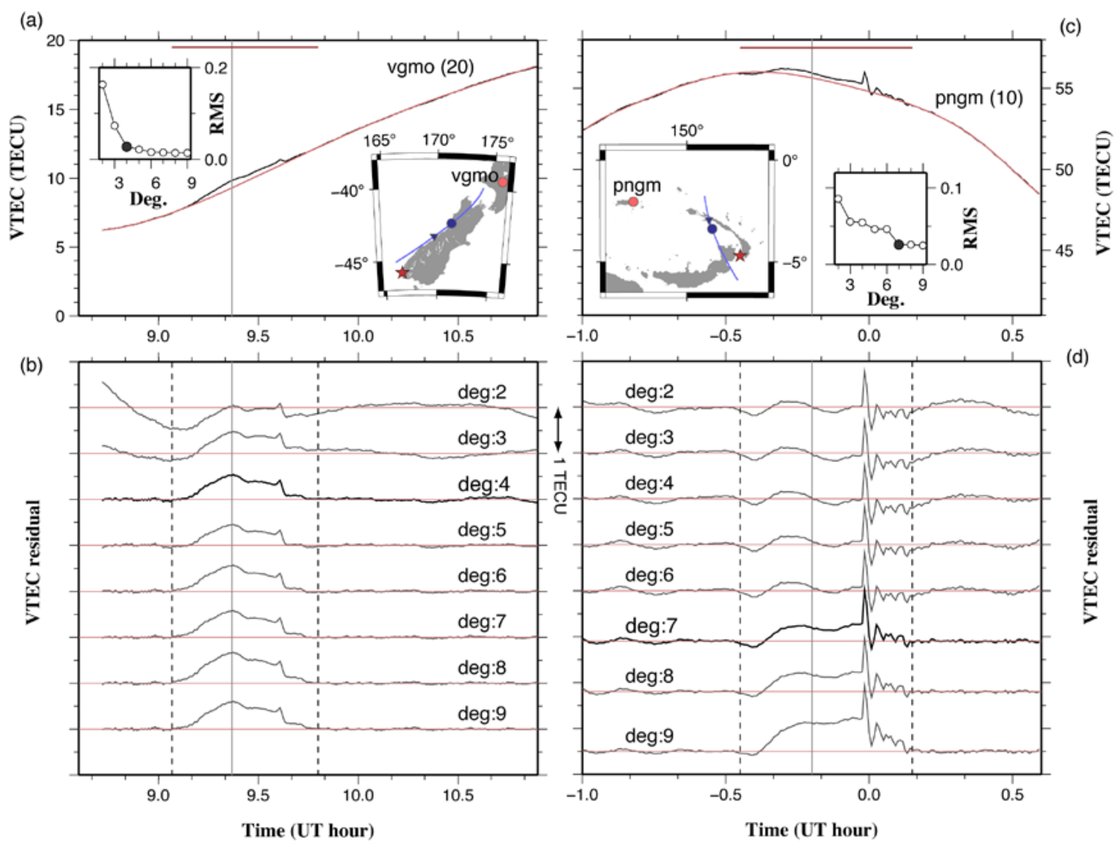

Figure 7. Fit of polynomials to the VTEC curves with prescribed excluding windows, for the 2009 July New Zealand earthquake (a,b) and the 2015 March Papua New Guinea earthquake (c,d). Assuming the exclusion windows, shown as red bars in (a), (c) and the vertical dashed lines in (b), (d), we fit the VTEC outside these windows using the polynomials with degrees 2 to 9. The residuals within the window are stable in the New Zealand case (b), but depend on the polynomial degree in the Papua New Guinea case (d). Small insets in (a) and (c) compare the root-mean-squares (RMS) for these polynomials. We considered the degree when RMS showed large drops the most appropriate one, as shown with black dots in the insets and with thicker curves in (b) and (d).

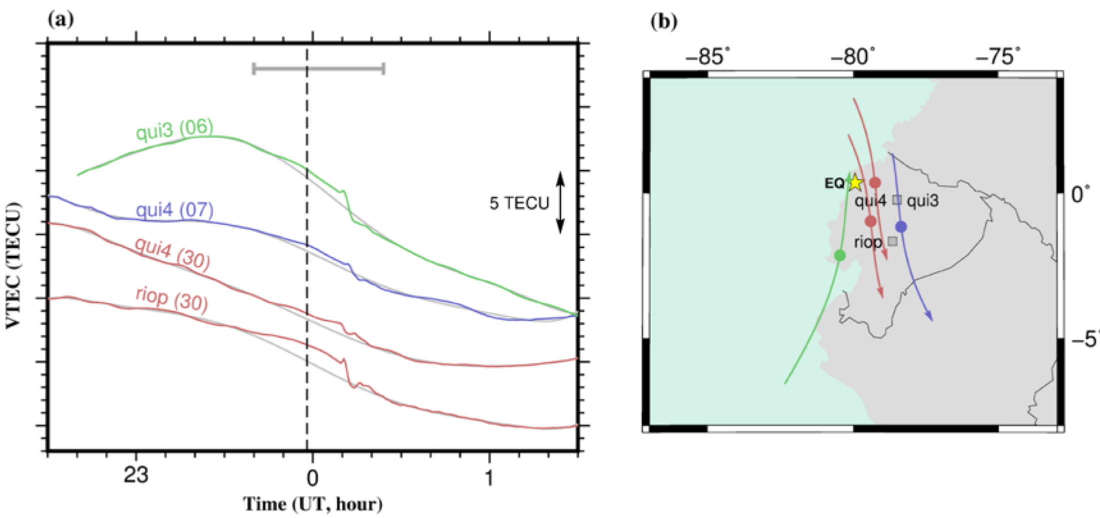

Figure 8. (a) Preseismic VTEC enhancements identified as the persistent positive departure from reference curves in four VTEC time series (thick curves) of different station-satellite pairs near the epicenter of the 2016 Ecuador earthquake. The horizontal gray bar at the top represents the time window (-18 minutes to +26 minutes) excluded in defining the reference curves (thin gray curves). Colors of the curves correspond to satellites. The vertical dashed line indicates the earthquake occurrence time. (b) SIP trajectories (same colors are used for same satellites) obtained by assuming the ionospheric height at 200 km. The circles on the trajectories show the SIP positions at the earthquake occurrence time. The yellow star shows the epicenter. SIP trajectories show the same time period as the VTEC change time series. We numbered the time series (a) and SIP trajectories (b) to show their correspondence.

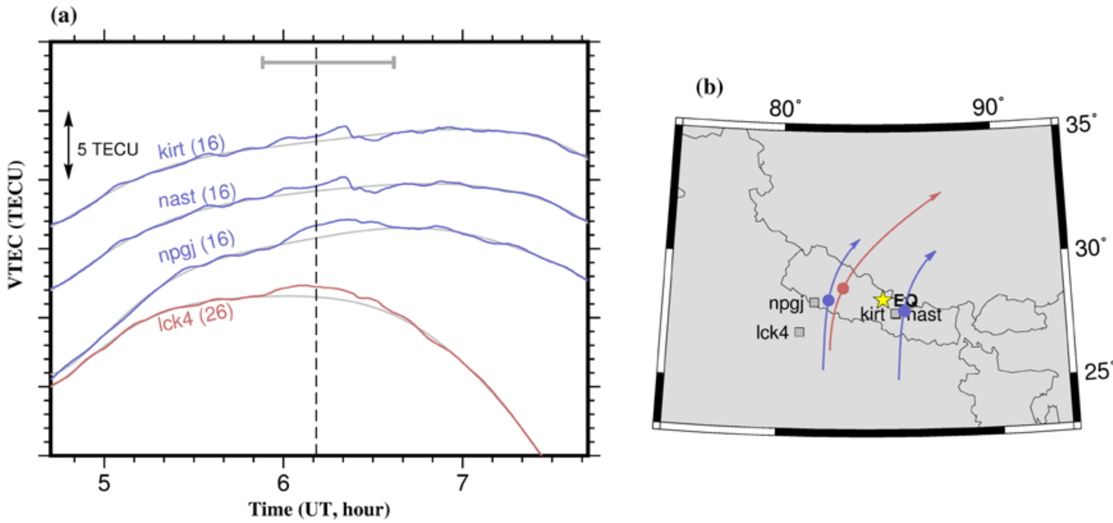

Figure 9. VTEC time series before and after the 2015 M_w7.8 Gorkha, Nepal, earthquake (mainshock) showing positive anomalies (a-1). For the horizontal gray bar and the vertical dashed line, see the caption of Figure 8. The maps show the SIP trajectories calculated assuming the ionospheric height of 200 km (a-2). For other symbols, see the caption of Figure 8. In order to show the decay of the precursor signatures with the epicentral distance, we also show examples of station-satellite pairs with SIP positions farther from the fault (b). The green rectangle in (b-2) indicates the approximate shape of the ruptured fault.

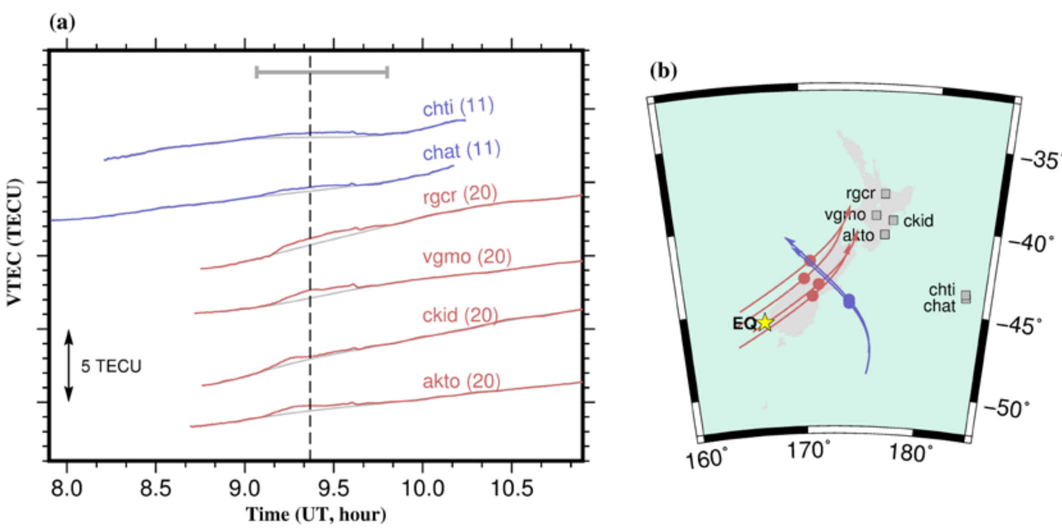

Figure 10. (a) Changes of VTEC before and after the 2009 M_w7.8 southern New Zealand earthquake. (b) SIP trajectories were calculated assuming the ionospheric height of 200 km. For other symbols, please see the caption of Figure 8.

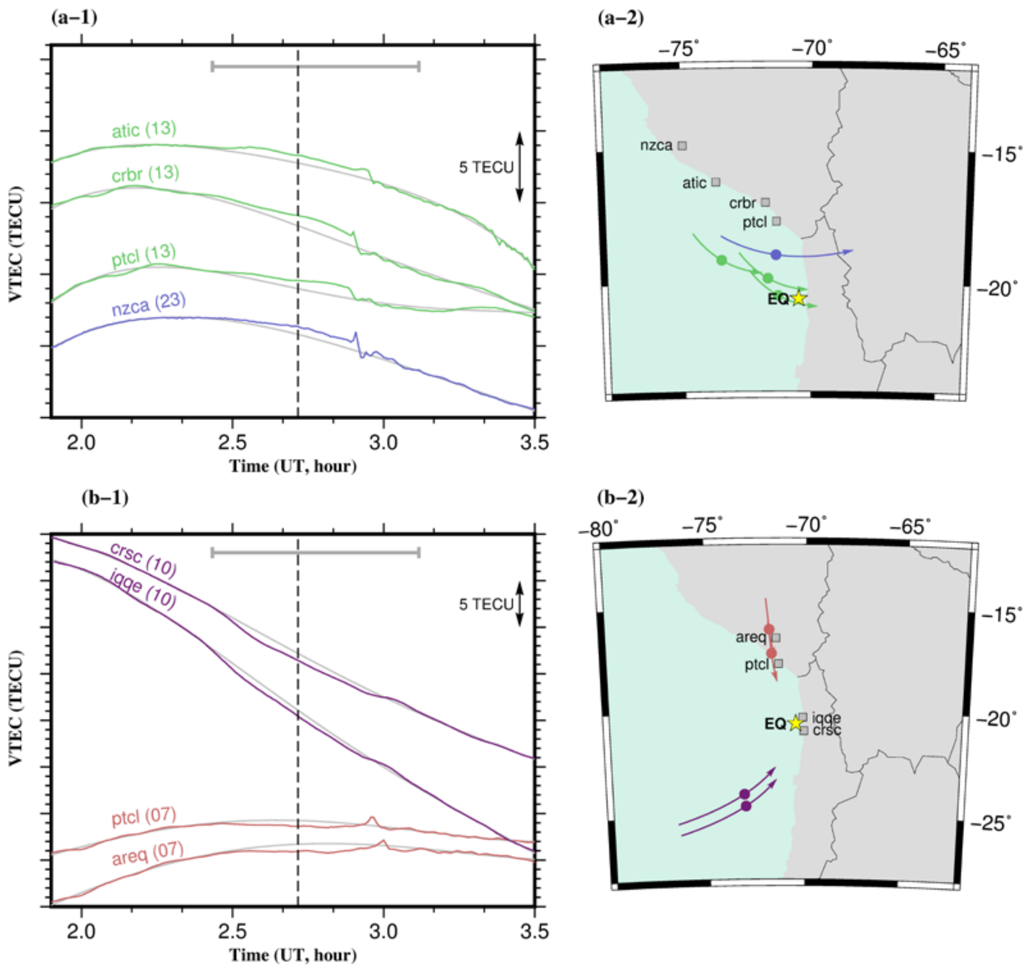

Figure 11. VTEC time series before and after the 2014 M_w7.7 aftershock of the Iquique earthquake showing positive (a-1) and negative (b-1) anomalies. The maps show the SIP trajectories for positive (a-2) and negative (b-2) anomalies assuming 200 km as the ionospheric height. For the other symbols, see the caption of Figure 8.

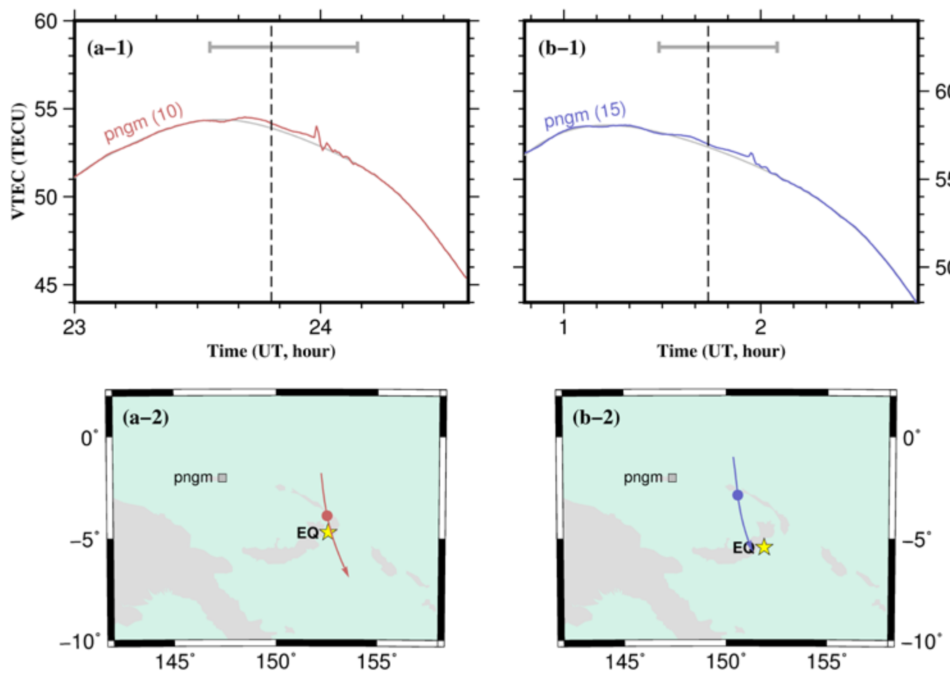

Figure 12. VTEC time series before and after the two M_w7.5 earthquakes in Papua New Guinea, on 29 March (a-1) and 5 May 2015 (b-1), 2015. We calculated the SIP trajectories in the maps assuming the ionospheric height of 200 km (a-2, b-2). For other symbols, please see the caption of Figure 8.

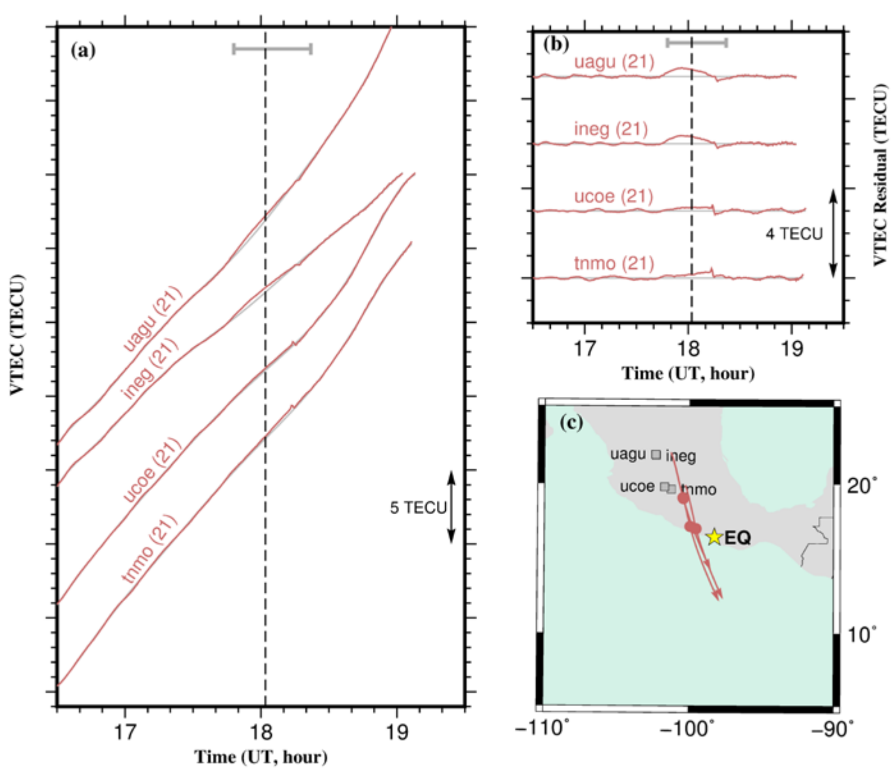

Figure 13. (a) VTEC time series before and after the 2012 March M_w7.4 Oaxaca earthquake, Mexico. Because of the high rate of VTEC, we plotted the VTEC residual in (b). The vertical dashed line represents the earthquake time. (c) The map showing the SIP trajectories calculated assuming the ionospheric height of 200 km. For other symbols, please see the caption of Figure 8.

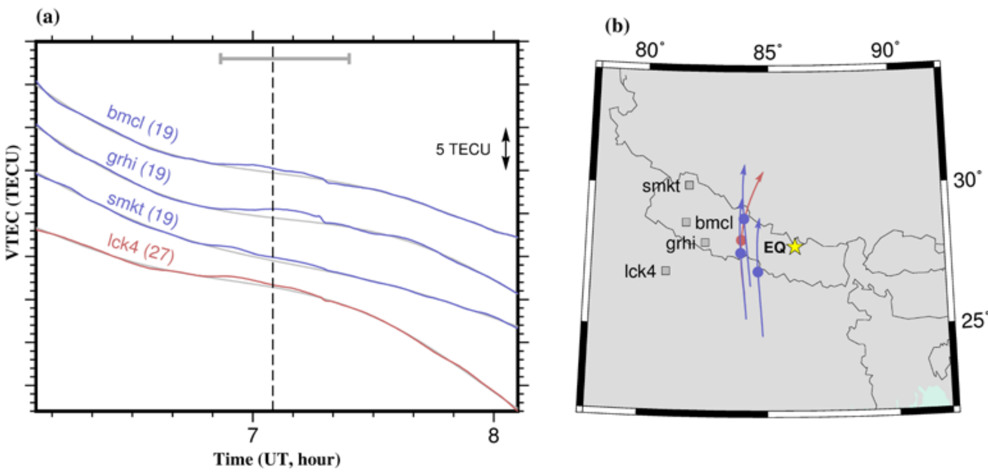

Figure 14. (a) VTEC time series before and after the M_w7.3 aftershock of the 2015 Gorkha, Nepal, earthquake. (b) The map showing the SIP trajectories calculated assuming the ionospheric height of 200 km. See caption of Figure 8 for other symbols.

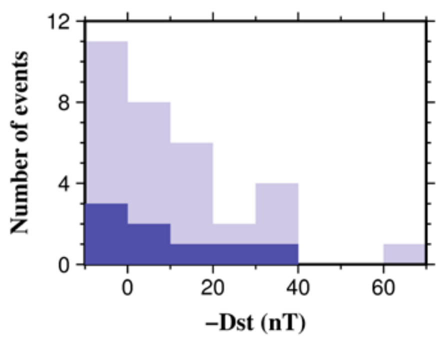

Figure 15. Two histograms of *D*st indices, i.e. all the 32 earthquakes studied here (light blue) and 8 earthquakes with possible precursory VTEC changes (dark blue). Their distributions are similar.

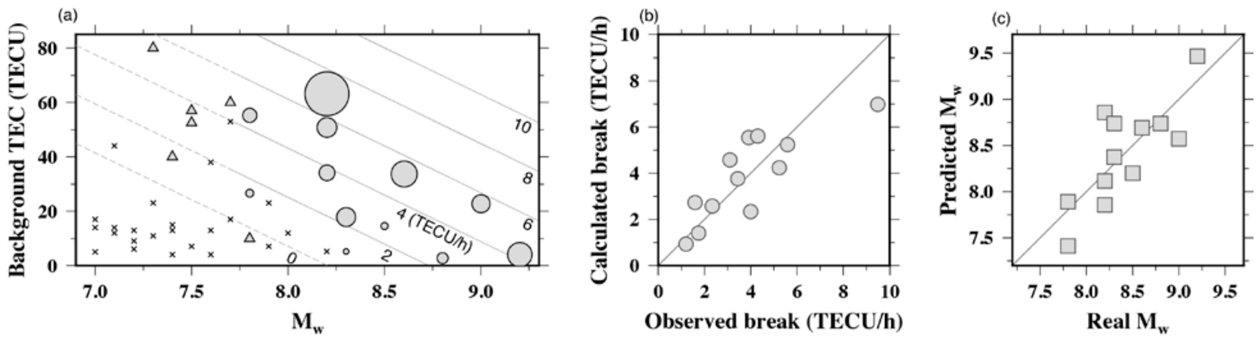

Figure 16. (a) Diagram showing the dependence of the preseismic VTEC rate changes (circle radius) on the background VTEC (vertical axis) and the earthquake M_w (horizontal axis), similar to Fig.4a of *Heki and Enomoto* [2015]. Six gray triangles represent the earthquakes, with the rate changes not large enough to calculate. Black crosses indicate earthquakes with no significant VTEC changes prior to earthquakes. We modeled the VTEC rate change (TECU/h), using the 12 earthquakes shown with circles, as 3.8 M_w + 0.11 VTEC – 31.3, and the contour lines show the same rate changes of 0, 2, 4, 6, and 8 TECU/h (dashed lines indicate parts not well substantiated by data). In (b) we compare observed VTEC rate changes and those calculated using this equation. In (c) we compare real M_w with those inferred by this equation from the background VTEC and the rate changes.

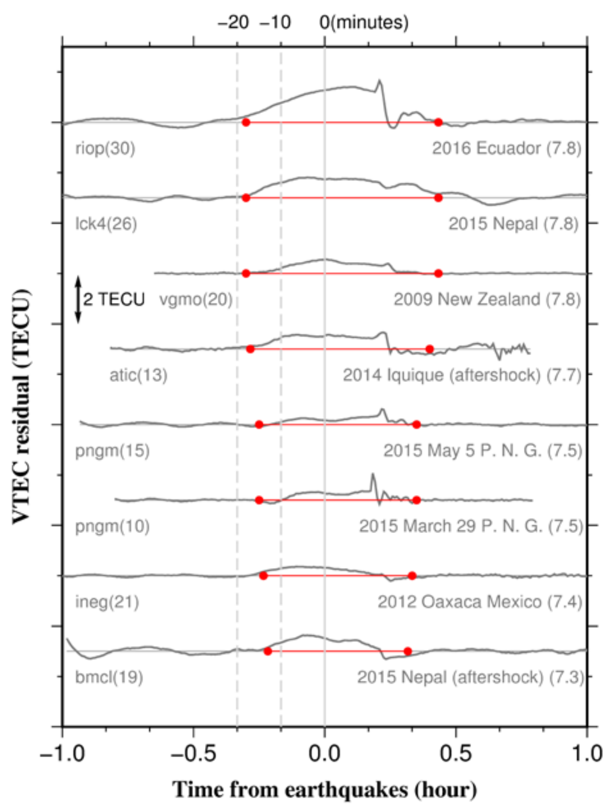

Figure 17. Comparison of the residual VTEC plots for the 8 earthquakes with possible precursors. Within the parentheses to the right of the curves, we indicate their M_w. To the left of the curves, we show station names and GPS satellite numbers. Two vertical dashed lines indicate

20 and 10 minutes before earthquakes. Red lines indicate the prescribed exclusion windows used in defining the reference curves.

Supporting Information

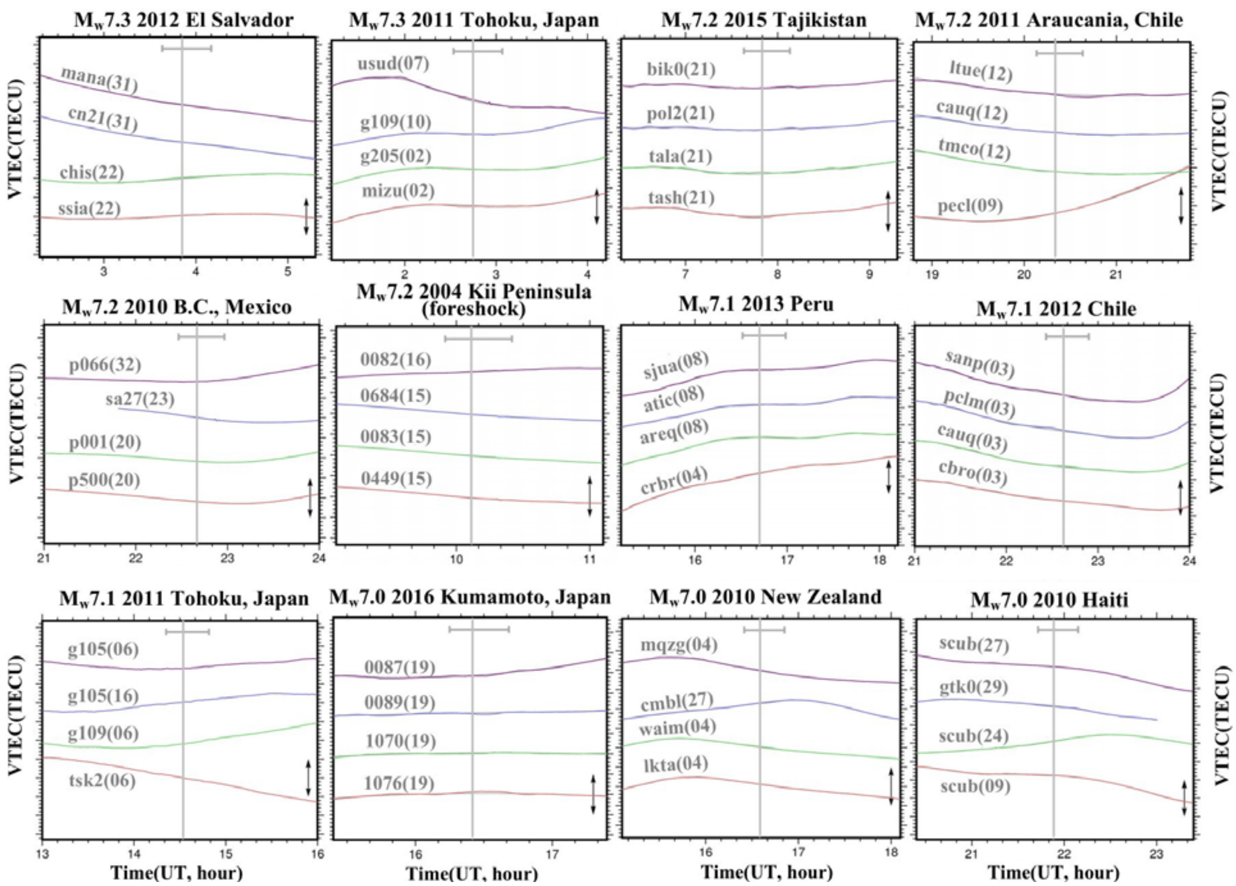

Figure S1. VTEC time series obtained from four station-satellite pairs near the epicenter, for 12 of the 24 earthquakes without preseismic anomalies (marked with symbol “x” in Table 1). The gray horizontal bars represent the excluded time period in defining the reference curves. The gray vertical lines represent the earthquake times. The vertical arrows represent 10 TECU. The degree of the polynomials used to model the reference curves are given in Table 1.

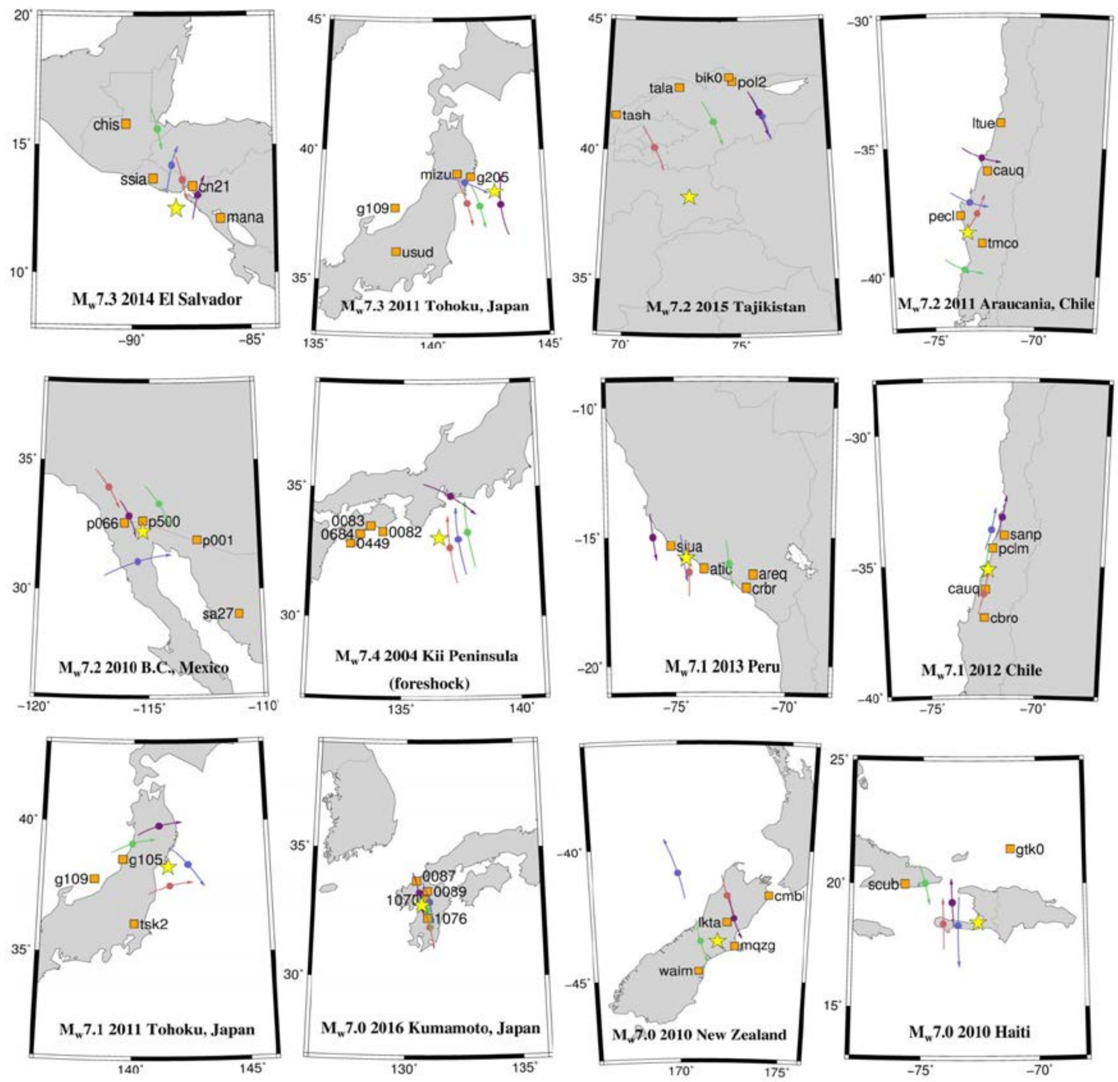

Figure S2. Maps showing the SIP trajectories (the same color for the same station-satellite pair in Figure S1) calculated assuming the ionospheric height of 200 km for 12 of the 24 earthquakes without precursory TEC changes (marked with symbol "x" in Table 1). The orange squares show the locations of GNSS stations. The colored circles on the SIP trajectories show the SIP at the earthquake time. The yellow stars show the epicenters.

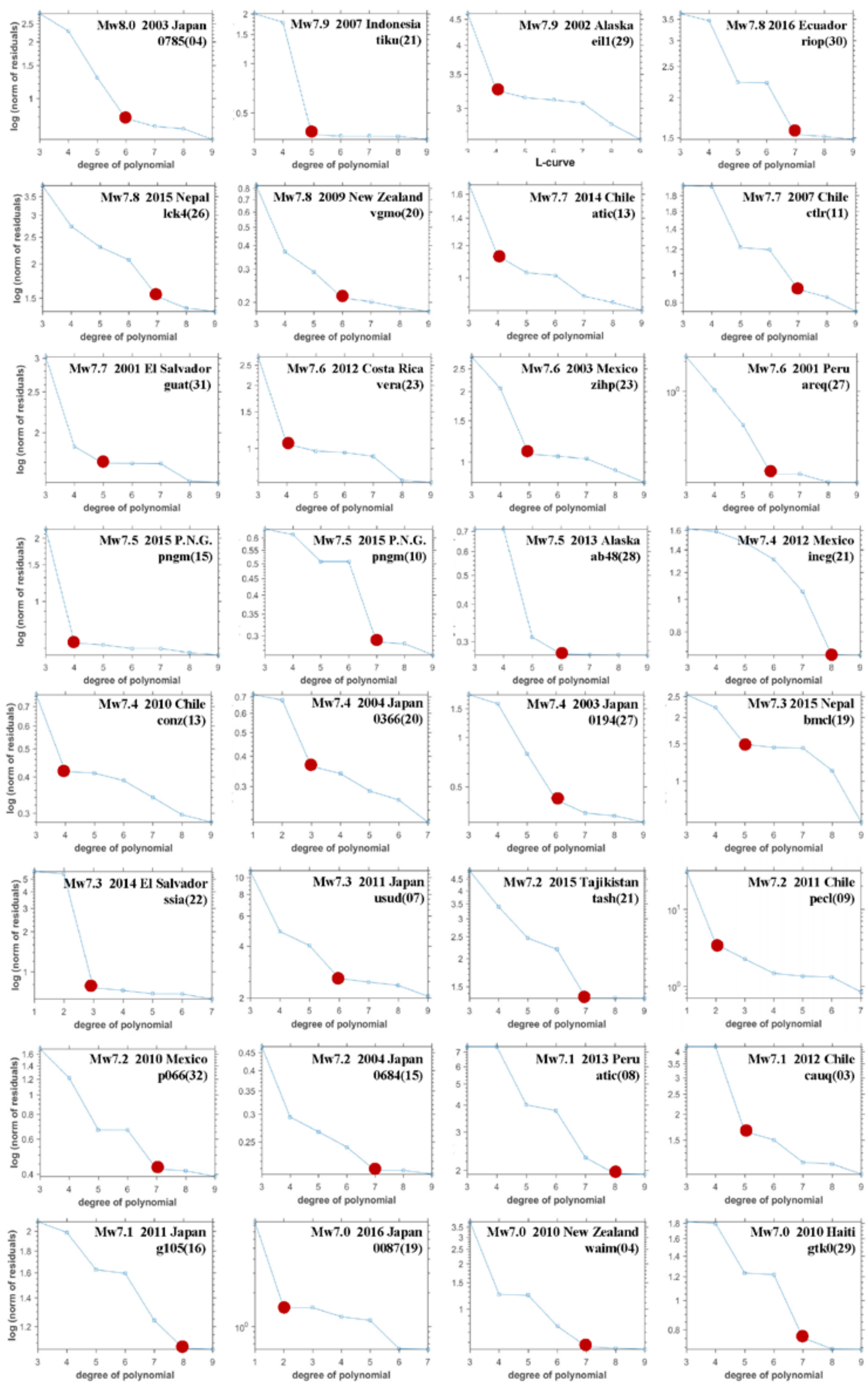

Figure S3. Behaviors of the post-fit residuals for various degrees of polynomials used to model the reference curves excluding certain windows before and after earthquakes. We employed the degrees marked with the red dots. The earthquakes are arranged in the same order as in Table 1.

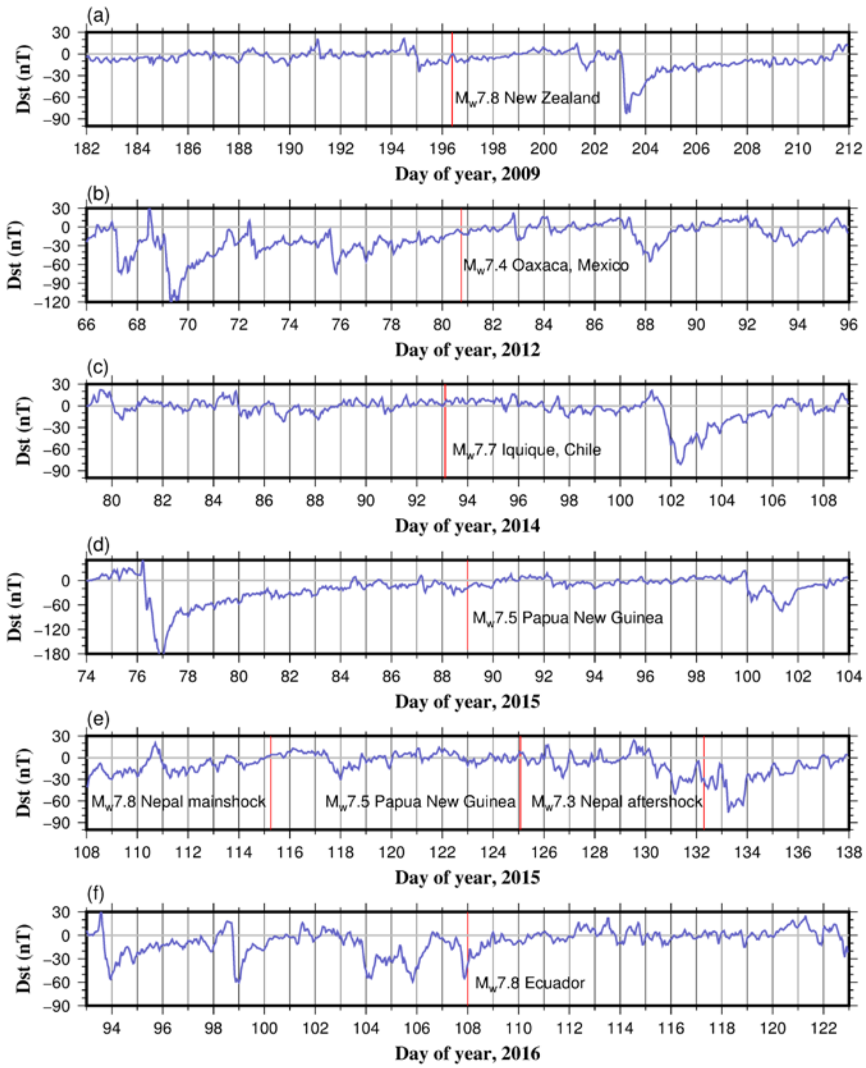

Figure S4. *D*st indices during 30-day periods before and after the 2009 New Zealand (a), the 2012 Oaxaca (b), the 2014 Northern Chile (aftershock) (c), the March 2015 Papua New Guinea (d), the 2015 Gorkha Nepal (mainshock), the May 2015 Papua New Guinea, and the 2015 Gorkha Nepal (aftershock) (e), and the 2016 Ecuador (f) earthquakes. The vertical red lines represent the earthquake occurrence times. Data downloaded from NASA/OMNIWeb (omniweb.gsfc.nasa.gov).

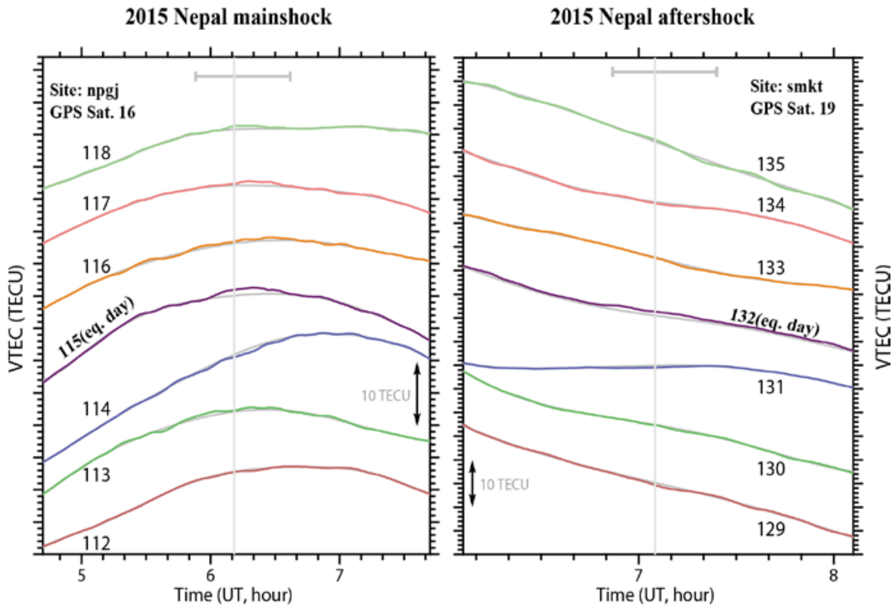

Figure S5. VTEC time series over seven consecutive days with the same pair of satellite-station for the 2016 Gorkha, Nepal, earthquake mainshock (a) and the largest aftershock (b). Although high background VTEC continues over these periods, we detect positive anomalies only on the earthquake days (day 115 for the mainshock and day 132 for the aftershock).

Table S1. The prescribed excluding time windows for earthquakes with M_w from 7.0 to 8.0 used in this study. Negative and positive times represent times before and after earthquakes, respectively.

M_w	Excluding time window (minutes)	
	Start	End
8.0	–20	+30 (10[*1] + 20[*2])
7.9	–19	+28 (10 + 18)
7.8	–18	+26 (10 + 16)
7.7	–17	+24 (10 + 14)
7.6	–16	+22 (10 + 12)
7.5	–15	+21 (10 + 11)
7.4	–14	+20 (10 + 10)
7.3	–13	+19 (10 + 9)
7.2	–12	+18 (10 + 8)
7.1	–11	+17 (10 + 7)
7.0	–10	+16 (10 + 6)

[*1]Time for acoustic waves to propagate to the F region and to make a hole, [*2]Time for LOS to escape from the electron depletion region (hole).